INVESTIGATION OF THE PLASMA ELECTROLYTIC OXIDATION MECHANISM OF TITANIUM

by

GOLSA MORTAZAVI

Presented to the Faculty of the Graduate School of
The University of Texas at Arlington in Partial Fulfillment
of the Requirements
for the Degree of

DOCTOR OF PHILOSOPHY

THE UNIVERSITY OF TEXAS AT ARLINGTON
July 2017

Acknowledgment

There were many people who helped make this research possible. First and foremost, I would like to thank Dr. Efstathios I. Meletis for all his guidance, patience and encouragement. His sincere interests in research and education have largely inspired me during the course of this research and will continue to be a source of aspiration throughout my life. I would like to extend my genuine gratitude to Dr. Jiechao Jiang for his invaluable help with characterization and microscopy techniques. I would also like to thank Dr. Choong-Un Kim, Dr. Pranesh Aswath, Dr. Harry F. Tibbals, and Dr. Seyedali Abolmaali for accepting to be members of my dissertation committee. I sincerely acknowledge all members of Surface and Nanoengineering Laboratory at UTA including Hsiao-Chien Wu, Randall Kelton, Anna Zaman and Hooman Rahmani for their help.

Abstract

Plasma electrolytic oxidation (PEO) is an environmentally friendly technology capable of forming coatings with excellent adhesion strength at high deposition rates. The PEO process is particularly attractive for forming desirable oxide-based coatings in transition metals (Al, Ti, Mg) to improve their surface sensitive properties. At present, the PEO mechanism is not fully understood since the process includes complex processes that are difficult to study. However, understanding the PEO mechanism is essential to produce coatings with desirable characteristics for a variety of new applications. One critical PEO process parameter is the applied total current to the workpiece. The total applied current in this process is composed of electronic current caused by sparking and ionic current caused by diffusion of electrolyte ions into the oxide. In the present work, a wide spectrum of current densities was applied on commercially pure titanium in alkaline electrolytes to investigate its effect on the voltage response and produced coating characteristics. The growth mechanism and oxide characteristics were investigated by studying the correlation between the ionic/electronic current contribution rate at different current densities during the PEO stages. The voltage-time response was found to be essential because it enables the quantification of the information about different PEO phases and correlate that information with the growth mechanism. It was found that at low current densities (30 and 40 mA/cm^2), the contribution of

electronic current is dominating and a large number of discharge channels develop in the oxide. However, in this case there would not be enough ions (low ionic current) to diffuse through the discharge channels for reaction. High density of plasma discharges at this condition, forms large number of discharge channels and increases the porosity and surface roughness of the coating. Also, these discharges provide enough energy to raise the temperature facilitating formation of both stable rutile and metastable anatase phases. By increasing the current density, the incorporation rate of ionic current increases which results in the formation of dense anatase coatings. It was found that in order to achieve high growth rates, an equal or balanced contribution from ionic (diffusion of ions for reaction) and electronic (generation of channels) charges is required. Transmission Electron Microscopy studies showed that all coatings are composed of two layers: an amorphous layer on the top produced by quenching from the electrolyte and a composite layer close to the substrate. The bottom composite layer has a complex microstructure consisting of nanocrystalline phases due to fast nucleation rate, amorphous structure and nano pores. The thickness ratio between the bottom complex layer and the top amorphous layer increases by increasing the applied current density. Thus, the present research revealed clearly that both the electronic and ionic current play a critical role in the PEO process and a balanced contribution is needed to realize the benefits in the oxide growth process. Furthermore, it is shown that electrolyte properties including composition and conductivity have significant

effects on breakdown voltage and contribution of the ionic charge and as a result coating characteristics.

Table of Contents

List of illustrations

List of Tables

Chapter 1

Introduction

1.1 Introduction and Motivation

Due to the unique combination of high strength to weight ratio, excellent biocompatibility and high corrosion resistance, titanium and its alloys are widely used in many industries such as aerospace, marine and biomedical [1, 2]. Poor wear resistance has traditionally restrained industrial applications of titanium; however, due to increasing technical demands, overcoming this limitation is an important field of research [3, 4].

Different surface treatment methods have been used to improve tribological properties of titanium and other light weight metals, include ion sputtering, electrodeposition, physical vapor deposition (PVD), etc. [5-9]. Even though each treatment has its own unique advantage, plasma electrolytic oxidation (PEO) treatments have become increasingly popular for developing hard ceramic coatings with high wear and corrosion resistance and excellent adhesion strength [10, 11]. This method relies upon creation of plasma microdischarges at the surface of a work piece electrode immersed in an appropriate electrolyte by applying a high voltage [12, 13].

To date, several investigations have been carried out on the effect of electrolyte composition [14-16] electrical modes [17-19], additives [20, 21] and temperature [22] on the surface morphology, corrosion resistance and wear properties of PEO coatings. For example, Shokouhfar et al. [23] have studied the effect of the electrolyte composition on the growth characteristics and corrosion behavior of ceramic coatings on titanium. Also, Terleeva et al. [24] investigated the effect of microplasma modes on the characteristics of PEO coatings on titanium for medical applications. Several other studies reported the effect of processing parameters on the produced coating characteristics and properties [25-28]. Despite these investigations that have been carried out so far, the mechanism of PEO is not fully understood due to the difficulty in probing the short lived plasma discharges specially at high current densities during the treatment [29, 30]. Therefore, in order to study the PEO mechanism and microdischarge characteristics in the present work, a spectrum of current densities was applied and the variation of voltage during the process for each current density was recorded. This method is helpful because it is easy to record and quantify the information about different PEO phases. This information can also be utilized to elucidate the growth mechanism and coating characteristics.

1.2 Research Objectives

The specific objectives of the present research are:

- Develop a fundamental understanding of the PEO mechanism by establishing a correlation between the relative contribution of the ionic/electronic currents and the produced coating characteristics. This is conducted by analyzing the voltage-time (V-t) behavior at different current densities.

- Understand the effect of electrolytes on ionic and electronic currents through the oxide via modification of the electrolyte conductivity.

- Use the knowledge gained of PEO mechanism to improve process controls and enhance surface sensitive properties of the produced coatings.

Chapter 2

Literature Review

2.1 Titanium Characteristics

As the ninth most abundant element in the earth's crust, titanium gained industrial attention and application relatively recently. Its commercial production began in 1948 fueled by the aerospace industry's demand for the unique high strength to weight ratio of titanium. Nevertheless, titanium offers other properties as well including high corrosion resistance and biocompatibility [31, 32].

As mentioned above, titanium alloys are particularly attractive for the biomedical industry because of their biocompatibility, followed by corrosion resistance. For instance, titanium alloys are widely used as hard tissue replacement such as artificial knee joint, artificial hip joints, bone plates, cardiac valve prostheses and screws for fracture fixation. The underlying reason for good biocompatibility of titanium is associated with its oxides. Titanium is naturally covered by a thin passive oxide layer which promotes biocompatibility through its physical properties: low electronic conductivity, low ion formation in aqueous environments and high resistance to corrosion [33].

Titanium has two allotropes, namely α and β forms. The α phase has hexagonal closed pack (HCP) and β has body centered cubic (BCC) structure. The α phase starts to change to β phase at 882 °C. Titanium can also be alloyed with different elements to form strong and tough alloys. Some of these elements like aluminum, carbon, nitrogen, and oxygen are α stabilizers and form strong alloys. Moreover, adding elements like molybdenum, vanadium, and zirconium promote formation of β alloys. Due to the BCC structure of β alloys, they are more ductile than the HCP α phase. Alpha- beta alloys have both types of stabilizers.Ti-6Al-4V, which is widely used in biomedical implants is in this group [34]. Table 2.1 and Table 2.2 summarize designations and physical properties of CP Ti and titanium alloys.

Table 2.1 Designation and nominal composition of some commercial titanium alloys [35].

Common alloy designation	ASTM grade	UNS designation	Nominal composition, wt%	Alloy type
CP 1(a)	1	R50250	Unalloyed titanium	α
CP 2(a)	2	R50400	Unalloyed titanium	α
CP 3(a)	3	R50550	Unalloyed titanium	α
CP 4	4	R50700	Unalloyed titanium	α
Ti-Pd(a)	7/11	R52400, R52250	Ti-0.15Pd	α
Ti-lean Pd(a)	16/17	R52402, R52252	Ti-0.06Pd	α
TIRU or TiRu(a)	26/17	R52404/R52254	Ti-0.1Ru	α
SMI-ACE(a)	30/31	…	Ti-0.3Co-0.05Pd	α
AKOT(a)	33/34	…	Ti-0.4Ni-0.015Pd-0.025Ru-0.15Cr	α
Grade 12(a)	12	R53400	Ti-0.3Mo-0.8Ni	α
Ti-3-2-5	9	R56320	Ti-3Al-2.5V	Near- α
Ti-3-2-5-Ru(a)	28	R56323	Ti-3Al-2.5V-0.1Ru	Near- α
Ti-3-2-5-Pd(a)	18	R56322	Ti-3Al-2.5V-0.06Pd	Near- α
Ti-6-2-1-1	…	…	Ti-6Al-2Nb-1Ta-0.8Mo	Near- α
Ti-5-2-5	6	R54250	Ti-5Al-2.5Sn	α
Ti-5-1-1-1	32	R55111	Ti-5Al-1Sn-1Zr-0.8Mo	Near- α
Ti-8-1-1	…	R54810	Ti-8Al-1V-1Mo	Near- α
Ti-6-2-4-2-S	…	R54620	Ti-6Al-2Sn-4Zr-2Mo-0.1Si	Near- α
Ti-6-4	5	R56400	Ti-6Al-4V	α -β
Ti-6-4-ELI	23	R56407	Ti-6Al-4V (0.13 max O)	α –β
Ti-6-4-Ru(a)	29	R56404	Ti-6Al-4V-0.1Ru (1.13 max O)	α –β
Ti-550	…	…	Ti-4Al-2Sn-4Mo-0.5Si	α –β
Ti-6-6-2	…	R56620	Ti-6Al-6V-2Sn-0.6Fe-0.6Cu	α –β
Ti-6-2-4-6	…	R56260	Ti-6Al-2Sn-4Zr-6Mo	α –β
Ti-6-22-22	…	…	Ti-6Al-2Sn-2Zr-2Mo-2Cr-0.15Si	α –β
Ti-17	…	R58650	Ti-5Al-2Zr-2Sn-4Mo-4Cr	α –β
Ti-10-2-3	…	…	Ti-10V-2Fe-3Al	Near- β
Ti-5-5-5-3	…	…	Ti-5Al-5Mo-5V-3Cr	Near- β
Ti-15-3-3-3	…	…	Ti-15V-3Sn-3Cr-3Al	β
Beta-C(a)	19	R58640	Ti-3Al-8V-6Cr-4Zr-4Mo	β
Beta-C/Pd(a)	20	R58645	Ti-3Al-8V-6Cr-4Zr-4Mo-0.06Pd	β
Ti-13-11-3	…	…	Ti-3Al-13V-11Cr	β
Beta-21S(a)	21	R58210	Ti-15Mo-2.7Nb-3Al-0.25Si	β
Ti15-5-3(a)	…	…	Ti-15Mo-5Zr-3Al	β
Ti45Nb	…	…	Ti-45Nb	β

Table 2.2 Physical properties of titanium [36].

Property		Value
Atomic number		22
Atomic weight (g/mol)		47.9
Crystal structure		
Alpha, hexagonal close packed		
c(Å)		4.6832±0.0004
α(Å)		2.9504±0.0004
Beta, cubic, body centered		
α (Å)		3.28±0.003
Density (gcm^{-3}), 0°C	c.p. titanium, Grade 2	4.5175
	B-titanium at 1000°C	4.302
	Amorphous titanium	3.54
Coefficient of thermal expansion, α, at 0-100°C (10^{-6} K^{-1})	c.p. titanium, Grade 2	16.3
Melting temperature (°C±15)	c.p. titanium, Grade 2	1668
Boiling temperature (°C)	High purity	3210
Phase transformation temperature (°C)	c.p. titanium, Grade 2	882.5
Electrical resistivity (μΩ cm)	High purity	42
	c.p. titanium, Grade 2	55
Modulus of elasticity (GPa)	c.p. titanium, Grade 2	103
Yield strength/Density (10^6N m kg^{-1})	c.p. titanium, Grade 2	78
Ultimate strength/Density (10^6 N m kg^{-1})	c.p. titanium, Grade 2	107
10^7 Cycle fatigue strength/Density (x10^6 N m kg^{-1})	c.p. titanium, Grade 2	54
Hardness, Bhn	c.p. titanium, Grade 2	160

The phase diagram of Ti-O is shown in Figure 2.1. As it is shown, oxygen has a large solubility in low-temperature α phase compare to the high-temperature bcc form, β Ti. At low temperature, Ti_2O, Ti_3O, and, possibly, Ti_6O are formed with some homogeneity range [37-39]. The stable condensed phase richest in O is rutile (TiO_2). Also, TiO_2 has two nonequilibrium phases namely, anatase and brookite, which will be discussed in the next section.

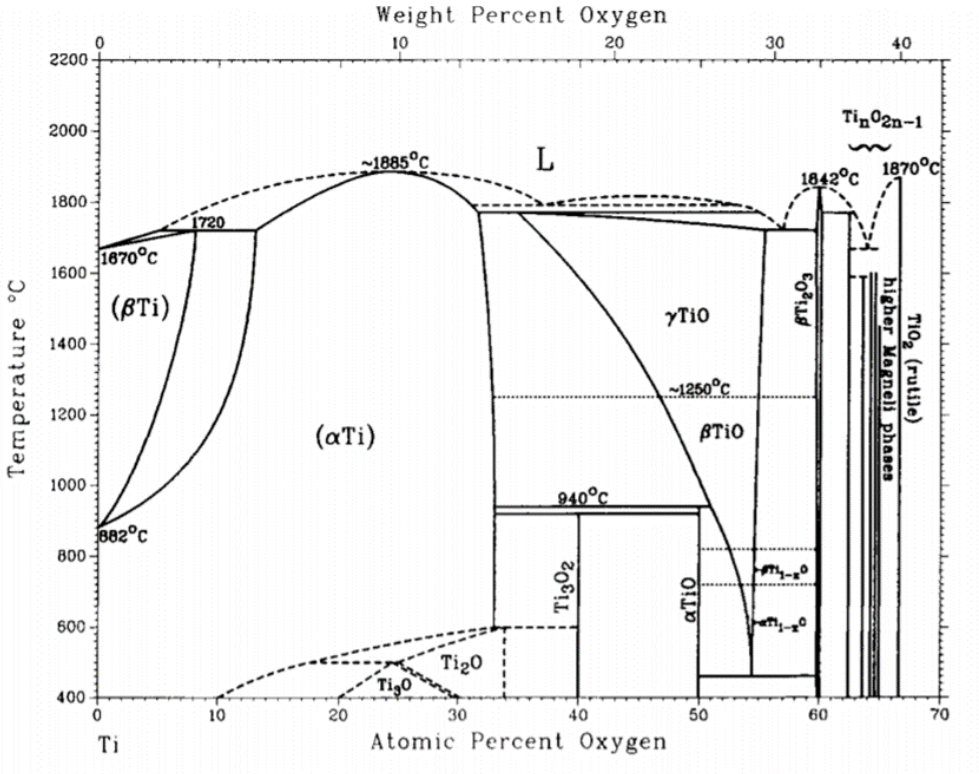

Figure 2.1 Phase diagram of Ti-O [39].

2.2 Titanium Oxide Characteristics

At ambient room pressure, titanium dioxide, aka titania, is the only naturally occurring form of oxide on titanium. This important wide-bandgap oxide has three polymorphs; rutile (tetragonal, a = 0.4593 nm, c = 0.2959 nm) which is the most stable form, anatase (tetragonal, a = 0.3758 nm, c = 0.9514 nm) and brookite (orthorhombic, a = 0.5436 nm, b = 0.9166 nm, c = 0.5135 nm) which are metastable [40-43]. As mentioned, these forms exist naturally at ambient pressure, however, at high pressures; five phases of TiO_2 have been reported [44, 45]:

- Cubic fluorite – type polymorph
- TiO_2 II or srilankite
- Pyrite type polymorph
- Monoclinic baddeleyite-type polymorph
- Continue type polymorph

  Anatase has tetragonal structure.

Anatase and rutile have tetragonal crystal structure, but the interfacial angles of the two minerals are completely different. Figure 2.2 presents the crystal structure of anatase and rutile phases of TiO_2. As it is shown six oxygen anions surround one titanium cation in rutile [46].

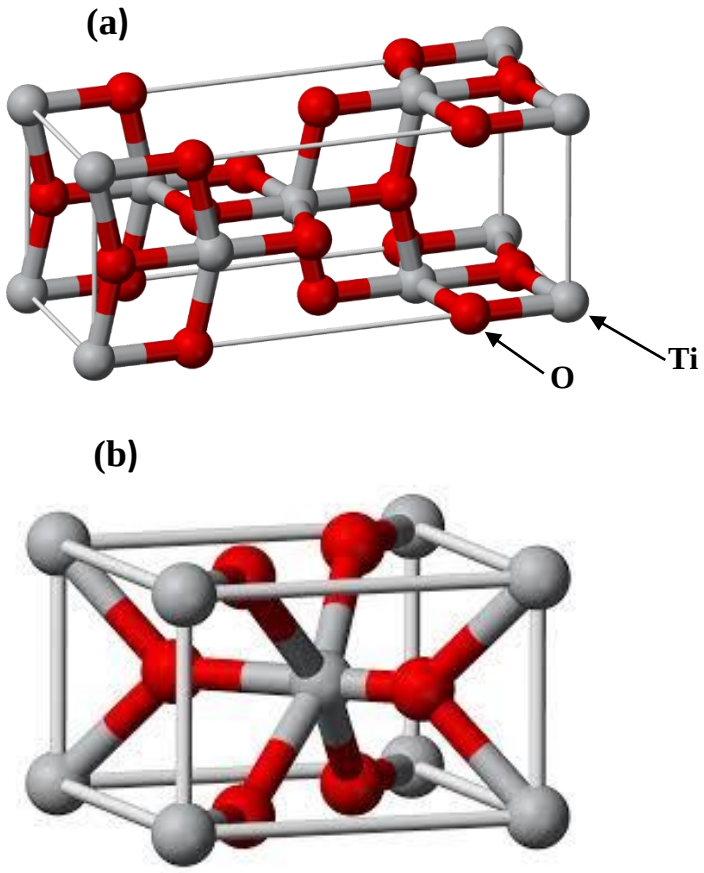

Figure 2.2. Crystal structure of (a) anatase and (b) rutile.

Thermodynamically, rutile is more stable than anatase, however, due to its kinetically favorable open structure, anatase is usually the product of titanium oxidation [47]. Therefore, at elevated temperatures denser and thermodynamically stable rutile forms whereas at low temperatures often less compact anatase is the product of oxidation [48]. This is because short-range ordered TiO_6 octahedra could arrange easier to long-range ordered anatase compared to the dense structure of

rutile. Additionally, although the Gibbs free energy of rutile is lower than anatase, its surface free energy is higher than anatase which results in slower recrystallization of rutile compared to anatase [49, 50]. However, it should be noted that through implementation of hydrothermal methods, it is possible to synthesize rutile at room temperature by direct precipitation of TiO_2 from liquid phase [51]. Depending on the method used, the resulting titania might be a mixture of either anatase, rutile and amorphous phases. For instance, room temperature sol-gel synthesis, could result in a titania product solely composed of amorphous phases in which hydrolysis of $TiCl_4$ is the underlying mechanism [52]. However, if PVD is used all phases – anatase, rutile and amorphous – could be obtained through deposition of evaporated Ti and its subsequent oxidation [53].

Compared to rutile TiO_2, anatase presents higher bandgap energy, higher degree of hydroxylation and lower capacity to adsorb oxygen [54, 55]. Anatase is a key component of injection process of photochemical solar cells with great conversion efficiency [56]. Thin films of anatase has been shown to have different electrical and optical properties than rutile; these films possess a wider optical absorption gap with smaller electron effective mass which enables charge carriers to have higher mobility [57]. Therefore, for solar cell applications, anatase is preferred over other polymorphs because of its higher electron mobility, light weight and low dielectric constant [58]. Tang et al. [59] have shown that at high doping concentrations, donor-band conduction of anatase thin films demonstrate a Mott transition to

metallic behavior which is indicative of a comparatively large radius of donor electron wave function in anatase. Additionally, by comparing optical absorption and photoconductivity spectra, they realized a higher optical absorption edge for anatase compared to rutile.

Metastable anatase can irreversibly transform to the stable rutile phase (ART). Temperature and time are two important factors in anatase to rutile transformation. Typically, the transition occurs between 600 to 1000 °C, this temperature can vary based on the concentration and nature of impurities and dopants, atmosphere, heating rate, etc. Also, since ART is a reconstructive process and bonds break and reform again it needs time and it is not instantaneous. In ART nucleation and growth occurs [47].

2.3 Fundamentals of Electrolytic Plasma Processing

Electrolytic Plasma Processing (EPP) is an electrochemical process involving electrolysis of an aqueous electrolyte accompanied by several electrode processes (Figure 2.3). The aqueous solution serves as a conductive bridge between two electrodes. Depending on the desired process, the workpiece can either be treated as the anode or cathode. In the anodic process, the sample is treated as an anode and non-metal deposition occurs and oxide forms on the sample surface. In the

cathodic process, the sample is the cathode with negative charge and either cleaning or deposition of metal species can take place. On the anodic surface, the liberation of gaseous oxygen and metal oxidation occur. Depending on the electrolyte chemical activity, the oxidation process can dissolve or form an oxide coating on the surface. On the cathodic surface, the liberation of gaseous hydrogen and cation reduction occur [13, 60]. A key aspect of the process is the creation of microdischarges which form fine channels at the surface of the working electrode through the application of a high voltage [61].

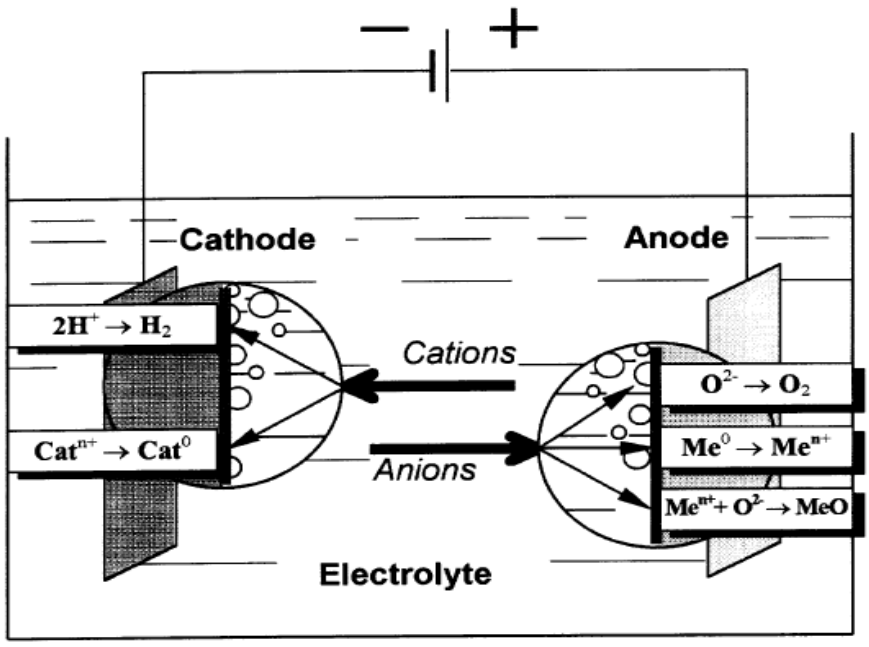

Figure 2.3 Electrode reactions in electrolysis of aqueous solutions [13].

Several process parameters can have an influence on the electrode reaction rate, including the electrode itself, electrolyte, mass transfer, electrical, and external ones . A schematic of the cell with these parameters are presented in Figure 2.4 [62, 63].

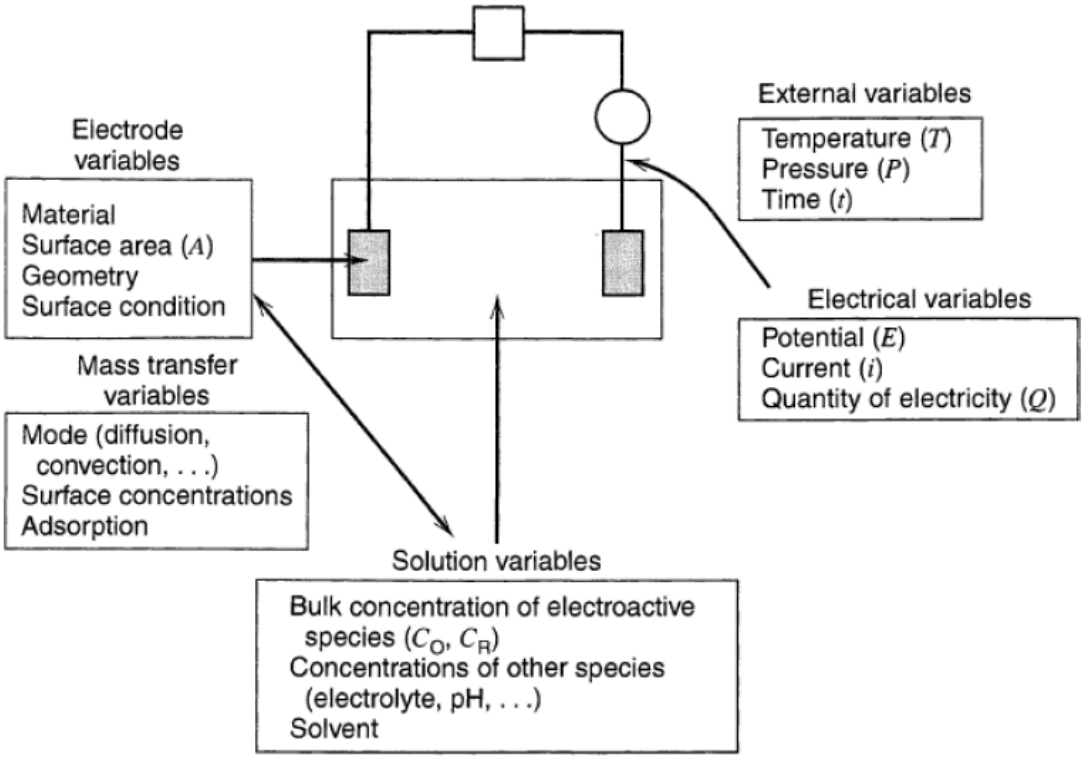

Figure 2.4 Variables influencing the electrode reaction rate [62].

The rate of an electrode reaction is proportional to the electrical charge passed through the interface in unit of time (current). In electrochemical literature, current is always used to express rate of an electrode reaction. Extent of this current depends on many factors including [62]:

1- Mass transfer of species towards the electrode
2- Chemical reactions happening before or after electron transfer reaction.
3- Kinetics of electron transfer at the electrode.
4- Other physical-chemical reactions on the surface such as adsorption, desorption and crystalization (electrodeposition).

Applied potential is a determinant variable for some of the processes mentioned above, e. g. electron transfer and adsorption depend on applied potential.

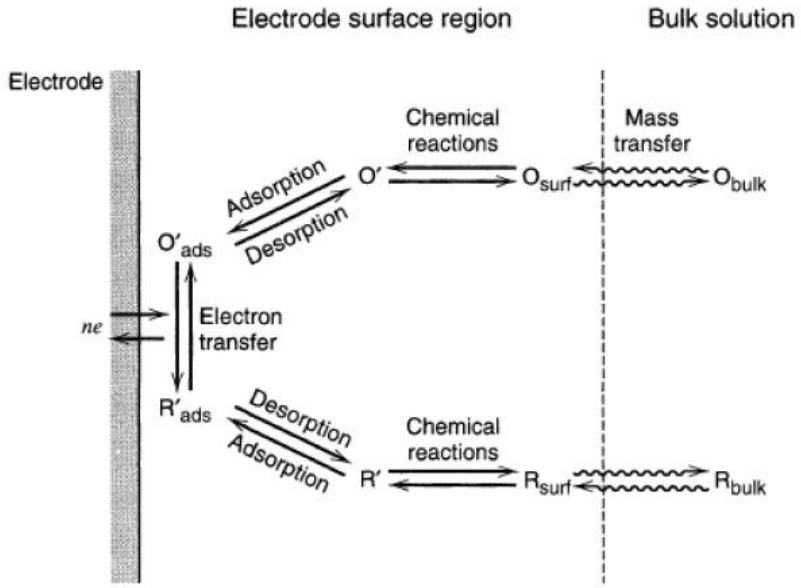

Figure 2.5 Pathway of a general electrode reaction.

Transfer of mass in the electrolyte arises either from concentration gradients or movement of a volume element of solution under electrical or chemical gradients. Therefore, three major modes of mass transfer are as follows:

1- Migration, movement of charged species under the influence of an electric field.
2- Convection: transfer of mass due to the bulk motion of units of volume within the electrolyte with an average velocity.
3- Diffusion: movement of species within the electrolyte caused by concentration gradients.

2.3.1 Cathodic Plasma Processing

Cathodic EPP which is also referred to plasma electrolytic saturation (PES) has been effectively used in cleaning and deposition of metal species. Cleaning of a metal surface is an important process prior to many applications such as coating and painting. Cleaning with PES yields the opportunity to remove the contaminants such as oxides, dirt, lubricants, etc. from the metal surface in an eco-friendly, one-step process. A $NaHCO_3$ electrolyte is typically used in the PES cleaning to form H^+ plasma and clean the surface. As it is shown in Figure 2.6(a) traditional acid pickling method needs multiples steps including cleaning, rinsing, pickling, etc. which is time consuming. However, cleaning the surface with PES can be done in just one step and it is much easier. Figure 2.6 shows a schematic of the required steps for acid pickling and PES cleaning [12].

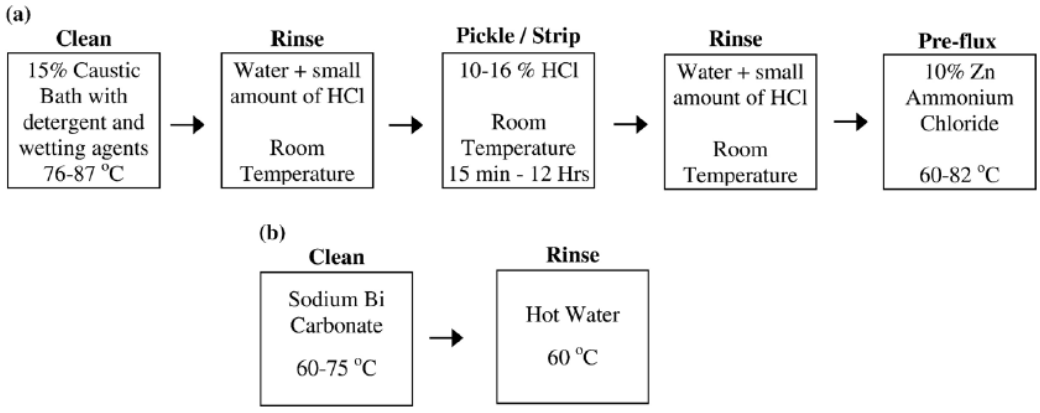

Figure 2.6 Required steps for (a) traditional acid pickling (b) PES cleaning [12].

PES can also be utilized to deposit coatings like Mo, Ni, Zn, Cu, and Al to improve surface characteristics such as corrosion, wear, etc. [64]. Previous work in the Surface and Nano Engineering Laboratory has shown that the difference in melting temperature between substrate and coating plays an important role in substrate/coating interface evolution [65]. Three coatings namely Mo, Zn, and Ni, were deposited on steel substrate by PES. It is shown that Zn with low melting point, developed intermetallics at the interface as expected by the phase diagram. In Ni coating which has similar T_m with steel substrate, a liquid phase with both soluble elements formed at the interface and based on the phase diagram substantial mixing occurred. The melting point of Mo is much higher than steel. These coatings revealed different morphology. Substrate extended far into the coating. Also, due to the difference in thermal expansion some cracks were present in Mo coating.

In another study, Smith et al. used PES to deposit Ni on low carbon steel substrate [64]. Dense nanocrystalline Ni with average grain size of 20 nm at a high deposition rate of 166 nm/s was formed on the substrate. It was shown that PES coated Ni increased corrosion resistance of the substrate significantly by decreasing the corrosion rate and increasing the corrosion potential. Also, electrochemical impedance spectroscopy results indicated that the corrosion mechanism of PES coated Ni is similar to the pure Ni. PES can be further utilized in carborizing,

carbonitriding, boronitriding, etc. A summary of selected studies that have been conducted on PES is presented in Table 2.3.

Table 2.3 Summarizing the recent investigations on PES.

Substrate	**Coating/ Process**	**electrolyte**	**Current mode**	**Voltage (V)**	**Duty cycle**	**Frequency (kHz)**	**Current density (A/cm^2)**	**Time**	**Temperature (°C)**	**Ref**
Pure Ti	Al	$Al_2(SO_4)_3$.$16H_2O$, $AlCl_3$	Pulsed bipolar DC	2000 cathodic 300 anodic	20% cathodic 60% anodic	1	-	-	-	[66]
Annealed CP-Ti	Carboboriding	Glycerol, borax, Boric acid	Pulsed bipolar DC	500-700 cathodic 200-400 anodic	$\frac{\text{Cathodic}}{\text{Anodic}} = 0.25$	10	0.5	-	40	[67]
6082 Al	Aluminum carbide	Glycerol based	Pulsed DC	400	5%	20	-	3-9 min	-	[68]
Low carbon steel (AISI 1010)	Zn and Zn–Al	$ZnSO_4$	DC	180-220	-	-	0.11-0.78	32 s	73	[60]
Stainless steel (AISI 316)	Nitrocarburizing	$(NH_2)_2CO$	DC	220–260	-	-	-	30-60 s		[69]
Low carbon chromium steel (AISI H13)	Nitrocarburizing Boronitriding Borocarburizing Borocarbonitriding	Carbamide Borax+Sodium nitride Borax + Calciu carbonate Carbamide + Borax	DC	Initial V< 150	-	-	-	15 min	-	[70]
Low carbon steel	Zn	16% $ZnSO_4$*7 H_2O	DC	170	-	-	3	30 s	-	[65]
Low carbon steel	Ni	20% $NiSO_4$*$6H_2O$	DC	200	-	-	3	30 s	-	[65]
Low carbon steel	Mo	10% Na_2MoO_4	DC	170	-		3	30 s	-	[65]
Low carbon steel	Ni	20% NiSO4	DC	200	-	-	2.6	10-30 s	75	[64]

2.3.2 Anodic Plasma Processing

Anodic plasma processing or PEO has tremendous advantages to form oxides on light metals such as Ti, Al, and Mg. This process can form hard, wear and corrosion resistant oxides on the metal surface at high deposition rates. PEO is similar to anodizing but higher potentials (400-700 V) are applied which results in generation of plasma discharges. Formation of these microdischarges produce high temperatures resulting in conversion of the substrate into the coating and production of high adhesion strength coatings [63, 71, 72].

2.4 Mechanism of Plasma Electrolytic Oxidation

During PEO, the work piece is surrounded by a continuous gas envelope of oxygen. High voltage between the electrodes in the electrolyte leads to the highly localized electric field. Due to this strong electric field, bubbles implode and gas space inside the bubbles is ionized, and a plasma discharge is initiated. It has been reported that, the plasma electric field strength can reach up to 10^5 V/m or higher. The temperature of the microdischarges is estimated between 8,000 to 10,000 K in the core and as high as 2000 °C at their surroundings [60, 61]. It is suggested that, high temperature of the plasma discharges lead to the localized melting of the

substrate close to the discharges and forming discharge channels. Also, anionic species present in the electrolyte enter these channels under the strong electric field and react with cations of substrate and forming oxides. During PEO processing, cations move outwards and oxygen ions and other anions move toward the substrate. Depending on the nature of the substrate, electrolyte, and mobility of ions, the inward and outward growth rate can change [73-75].

2.4.1 Plasma Discharge Generation Models

The plasma discharge duration is expected to be about 30 ms for each individual event. These microdischarges play a crucial role in the coating growth mechanism. Since plasma discharge have short lived, it is very hard to catch them instantly to examine the plasma processes in the channels. Therefore, there are some disagreements over the PEO mechanism.

Hussein et al. [61] used optical emission spectroscopy to study the discharge behavior of Al during PEO. They proposed three discharge models (Figure 2.7) Type B discharges is attributed to the dielectric breakdown by the strong electric field throughout the oxide. Type A and C discharges form at the micropores in the oxide. Type A discharge forms at the micropores located at the surface of the oxide, but Type C discharge occurs in relatively deep micropores. It is shown that the

strongest signal peaks correspond to the B type discharges which likely have penetrated the PEO oxide layer down to the coating/substrate interface

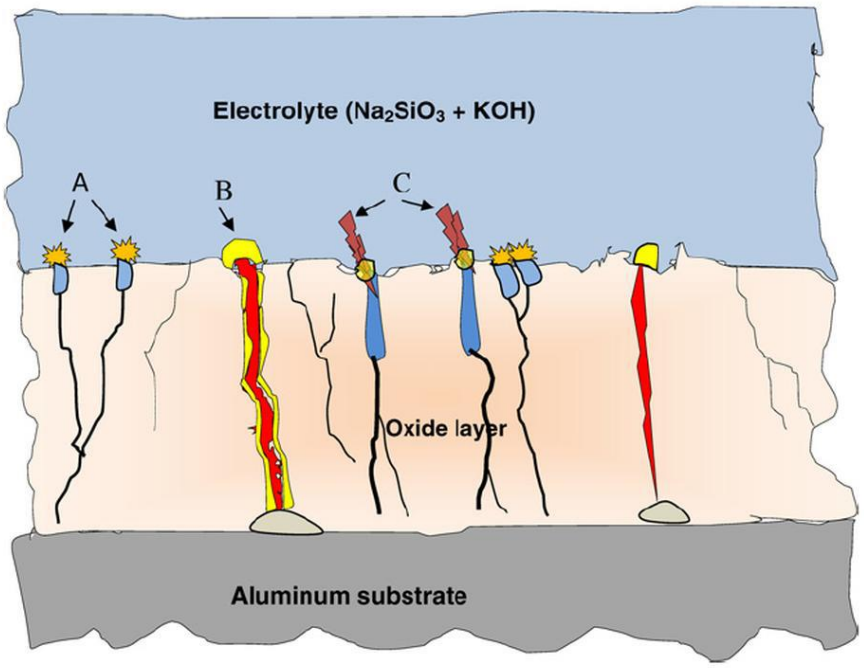

Figure 2.7 Schematic diagram of the discharge models for the PEO process for an Al sample [61].

Real time imaging has also been employed to study the micro discharge characteristics during PEO of titanium [76]. It is shown that at 20 mA/cm^2 relatively 100 cm^{-2} s^{-1} plasma discharges form on the sample surface in orthophosphate electrolyte. The size and lifetime of microdischarges range between ~70 - 380 μm

and ~35 - 800 ms, respectively. In their study, the lifetime of microdischarges has increased with treatment time. Pores may be formed due to the evolution of plasma discharges during growth.

2.5 Processing Parameters in PEO

Most of the studies have been conducted so far on PEO cover the effect of processing parameters on coating characteristics in different electrolytes under different regimes. A summary of many works on PEO of CP Ti and one of its popular alloys Ti- 6Al-4V, is summarized in Table 2.4. As it is shown, in terms of current mode, alternative current (AC), direct current (DC), and pulsed DC have been employed to form oxides. In terms of electrolyte, alkaline solutions are typically used in PEO and phosphate, borate, citrate, and carbonate electrolytes are among electrolytes are usually used in this process. Also, as it is presented, other processing parameters such as substrate, current density, treatment time, and temperature affect produced coating characteristics (thickness, mean roughness (R_a), phases, etc.).

Table 2.4 Summarizing the recent investigations on titanium and its alloys by PEO.

Ref	Substrate	Electrolyte	Current mode	Current density (mA/cm^2)	Time (min)	Thickness (μm)	R_a (μm)	Oxide
[15]	CPTi	Phosphate+ KOH	AC	300	8	5	NS	27%Rutile+Anatase
[15]	CPTi	Phosphate+ Borate+ KOH	AC	300	8	7	NS	29%Rutile+Anatase
[15]	CPTi	Phosphate+ Citrate+ KOH	AC	300	8	11	NS	41%Rutile+Anatase
[15]	CPTi	Phosphate + Silicate+ KOH	AC	300	8	9	NS	32%Rutile+Anatase
[77]	CPTi	Phosphate +KOH	DC	150	8	42	NS	27%Rutile+Anatase
[77]	CPTi	Phosphate +KOH+ Carbonate	DC	150	8	53	NS	54%Rutile+Anatase
[77]	CPTi	Phosphate +KOH+ Nitrate	DC	150	8	47	NS	31%Rutile+Anatase
[77]	CPTi	Phosphate+ KOH+ $CO(NH_2)_2$	DC	150	8	39	NS	22%Rutile+Anatase
[78]	CPTi	Aluminate + NaOH	Pulsed DC	30-100	40	12-24	7-9	Rutile +Anatase
[79]	TA1	$Ba(OH)_2$	AC	200-500	20	-	-	$BaTiO_3$
[80]	CPTi	Phosphate+ KOH	AC	200	NS	NS	10	Rutile +Anatase
[80]	CPTi	Phosphate+ KOH	AC	200	NS	NS	8	Rutile +Anatase
[81]	Ti_6Al_4V	Sodium aluminate+ Calcium hypophosphite	DC	200	15	3	0.32 -1	Al_2TiO_5 +$AlPO_4$+TiO_2
[82]	Ti_6Al_4V	NaH_2PO_4+ K_2ZrF_6	AC	200	50	80-150	6.2-6.7	$KZr_2(PO_4)_3$ +t ZrO_2+m- ZrO_2+ ZrP_2O_7
[83]	Ti_6Al_4V	Aluminate	DC	200	NS	60	3-4	Al_2TiO_5 + Al_2TiO_5.TiO_2
[23]	CPTi	Carbonate+ KOH	Pulsed DC	350V	3	8	NS	Rutie+ Anatase
[23]	CPTi	Aluminate+ KOH	Pulsed DC	350V	3	5.2	NS	Al_2TiO_5+Anatase
[23]	CPTi	Aluminate+ Fluoride	Pulsed DC	350V	3	5	NS	Al_2TiO_5+Anatase
[23]	CPTi	Aluminate+ Fluoride+ KOH	Pulsed DC	350V	3	3.1	NS	Anatase+Rutile
[4]	Ti–15V–3Al–3Cr–3Sn	Phosphate+ Aluminate+ Sulfuric acid+ Phosphoric acid	Pulsed DC	200	6	15	NS	Al_2TiO_5+Rutile+ γAl_2O_3
[84]	Ti_6Al_4V	Phosphate+ Aluminate	AC	200	60	20-40	2.8	Al_2TiO_5 +Rutile+ Al_2O_3
[85]	Ti_6Al_4V	Phosphate+ Aluminate	Bipolar pulsed DC	200	60	60	5.3	Mostly Al_2TiO_5

[85]	Ti_6Al_4V	Phosphate+ Aluminate+ Silicate+ KOH	Bipolar pulsed DC	200	60	13	4.1	TiO_2: Al_2TiO_5~1:1
[85]	Ti_6Al_4V	Silicate+ NaOH	Bipolar pulsed DC	200	60	60	10.4	SiO2: TiO_2~4:1
[85]	Ti_6Al_4V	Phosphate+ Silicate+ KOH	Bipolar pulsed DC	200	60	35	15	TiO_2: Al_2TiO_5~1:1
[86]	Ti_6Al_4V	Phosphate	Pulsed DC	800	120	15	-	TiO_2
[86]	Ti_6Al_4V	Phosphate +K_4 ZrF_6	Pulsed DC	800	120	100	-	ZrP_2O_7, $mZrO_2$, t-ZrO_2, ZrTiO4
[86]	Ti_6Al_4V	Phosphate+ Aluminate	Pulsed DC	800	120	160	-	Al_2TiO_5, Al_2O_3, TiO_2

2.5.1 Electrolyte Composition

Different types of electrolytes can be used in producing oxide coatings on titanium under different regimes. Electrolytes that can be utilized in generating of oxide coatings on metal surface in PEO process may be divided into four common categories:

1. Electrolytes that dissolve metal fast.

2. Electrolytes that dissolve metal slowly.

3. Electrolytes that slightly passivate metal.

4. Electrolytes that strongly passivate metal.

Electrolytes from groups (3) and (4) allow the sparking voltage to be easily reached and are the most helpful for coating formation by PEO [14, 87]. These electrolytes can only add oxygen into the oxide or they can add anions and cations in addition to oxygen.

Since electrolyte composition plays a significant role on coating characteristics, many studies have been conducted in this area. Here, some of these investigations were summarized. Surface characteristics of coatings produced in nine different electrolytes were compared and put in three groups. First coatings prepared in, (sodium silicate (NS), sodium phosphate (NP), and sodium borate (NB)) based electrolytes [14], second, (sodium aluminate (NA), sodium carbonate (NC) and calcium carbonate (CC)) and third, (NA, NA+ sodium fluoride (NF), NF+ KOH (NKF)) based electrolytes [23] were studied. In conclusion, the growth rate and differences of the coatings formed in these electrolytes were compared. These coatings produced at 350V with frequency of 1000Hz and duty cycle of 40% for 3 minutes.

First, three kinds of electrolyte, namely NS, NP, and NB were used to determine the influence of the electrolyte composition on the surface properties of PEO coating, Figure 2.8 [14]. It is suggested that voltage in which plasma discharge events start to happen or sparking voltage has a significant role on surface morphology, size and uniformity of pores, thickness and corrosion resistance of

coatings. Increasing sparking voltage might lead to an increase in plasma discharge energy and thus formation of larger non-uniform pores. Figure 2.8 (a) and (b) shows the coatings produced in NS and NP electrolytes had a pancake shape structure due to the formation of plasma discharges which leave behind porosity after cooling the coating.

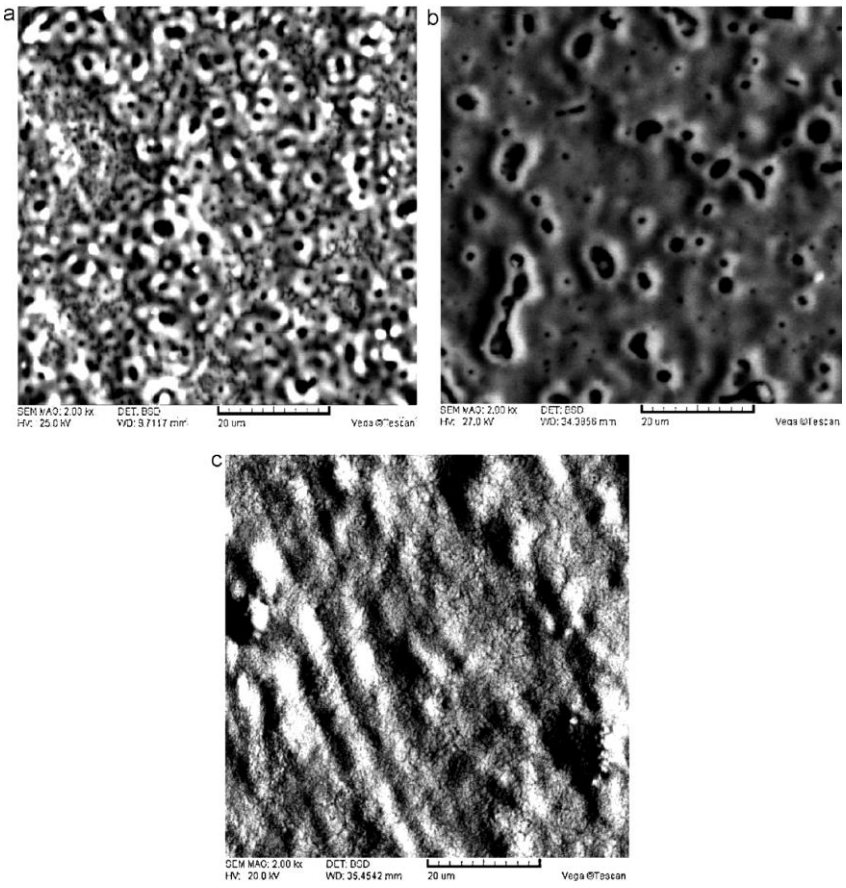

Figure 2.8 Surface morphology of PEO coatings prepared in (a) NS; (b) NP; and (c) NB electrolytes [14].

The coating produced in NP electrolyte showed higher sparking voltage (310 V) and exhibit larger pores, compared to the coatings formed in NS electrolyte with sparking voltage of 290 V. No sparking was seen in borate based electrolyte (NB), and produced coating was very dense and thin, which is shown that the applied voltage might not be enough in CC electrolyte to form plasma discharges

Second, surface characteristics of the coatings prepared in CC, NC and NA electrolytes were investigated [23]. Figure 2.9 shows different surface morphologies for these coatings. Pancake structure was not seen in the surface morphology of the coating prepared in CC electrolyte similar to the coatings produced in NB, Figure 2.9(a). Coatings formed in NC and NA electrolytes have sparking voltage of 310V and 270V, respectively and show pancake structures which attributed to the development of plasma discharges on the surface. The coating fabricated in NC, Figure 2.9(b), had large number of non- uniform pores, but coatings prepared in NA, Figure 2.9(c), exhibited fine and uniform pores. These differences might also be attributed to the different sparking voltages. Moreover, coatings produced from aluminate based electrolyte showed a better corrosion resistance than the carbonate based electrolyte.

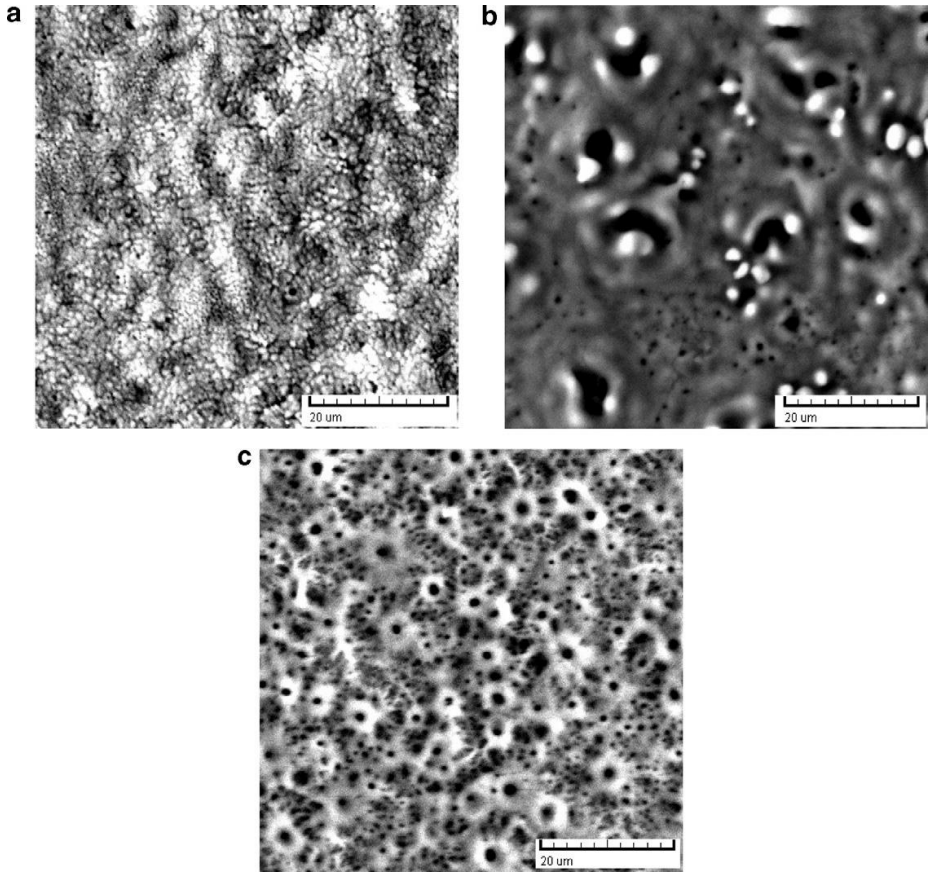

Figure 2.9 Surface morphology of PEO coatings (×2000) prepared in (a) CC; (b) NC; and (c) NA electrolytes [23].

It is suggested that lower porosity level, also presence of $TiAl_2O_5$ in addition to TiO_2 phases (rutile and anatase) coatings fabricated in NA electrolyte might have influence on increasing the corrosion resistance of the coating. All the coatings significantly improved corrosion behavior of titanium.

Finally, the effect of the addition of NaF and KOH to NA electrolyte was investigated, Figure 2.10 [23]. All of these coatings have sparking voltage about 270 V, but as it is shown in Figure 2.10(c) the addition of NaF lead to the formation of non-uniform pores. During the PEO process, fluoride ions in the electrolyte partially become hydrofluoric acid (HF) which has detrimental effect on the coating surface [23].

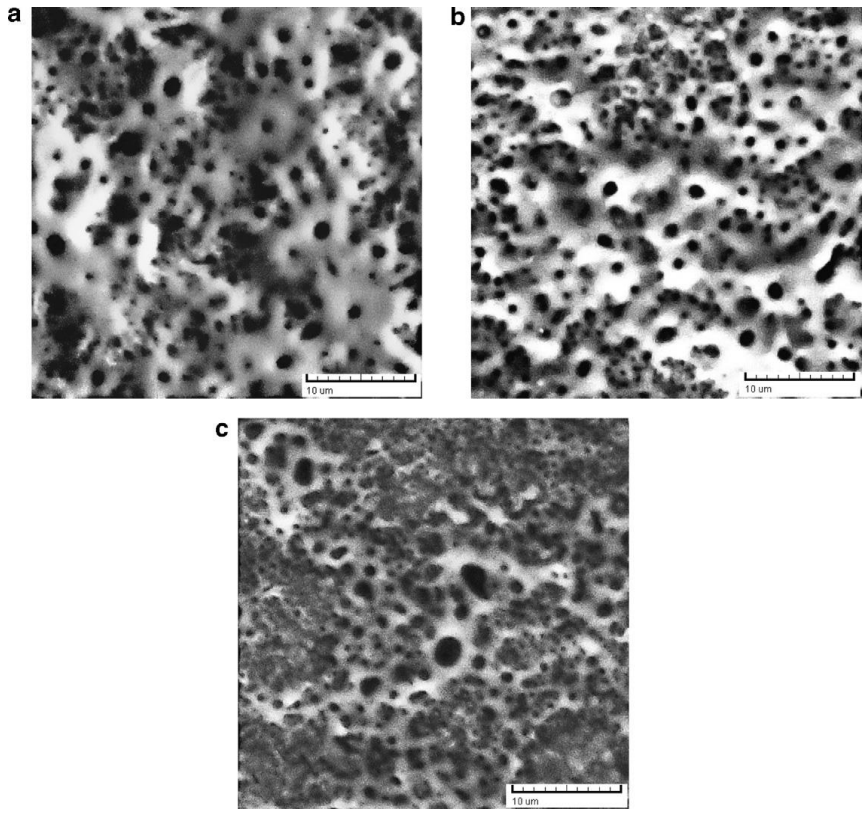

Figure 2.10 Surface morphology of PEO coated samples (×4000) prepared in (a) NA; (b) NKF; and (c) NF electrolytes [23].

It is also shown that incorporation of fluoride ions into the oxide by formation of titanium- fluoride compounds can also decrease the adhesion strength of the coating to the titanium substrate [87]. Pores are more uniform in coatings produced in NKF than NF electrolyte, Figure 2.10(b), suggesting that presence of KOH is beneficial for developing a uniform structure.

The thickness of the coatings produced in different electrolytes using constant pulsed DC current is presented in Figure 2.11 [14, 23]. Coatings produced from NB and CC electrolytes are thinner due to the fact that no plasma discharges developed during the process. A coating formed in NC electrolytes had a thicker coating than that of a coated sample produced in NA electrolyte which can be attributed to the higher sparking voltage for that sample. The resultant coating produced in NF electrolyte, is approximately as thick as that for the sample in NA electrolyte. However, the NF coating adhesion to the substrate is the weakest among the other samples. The coated sample in NP electrolyte has the highest growth rate among other electrolytes.

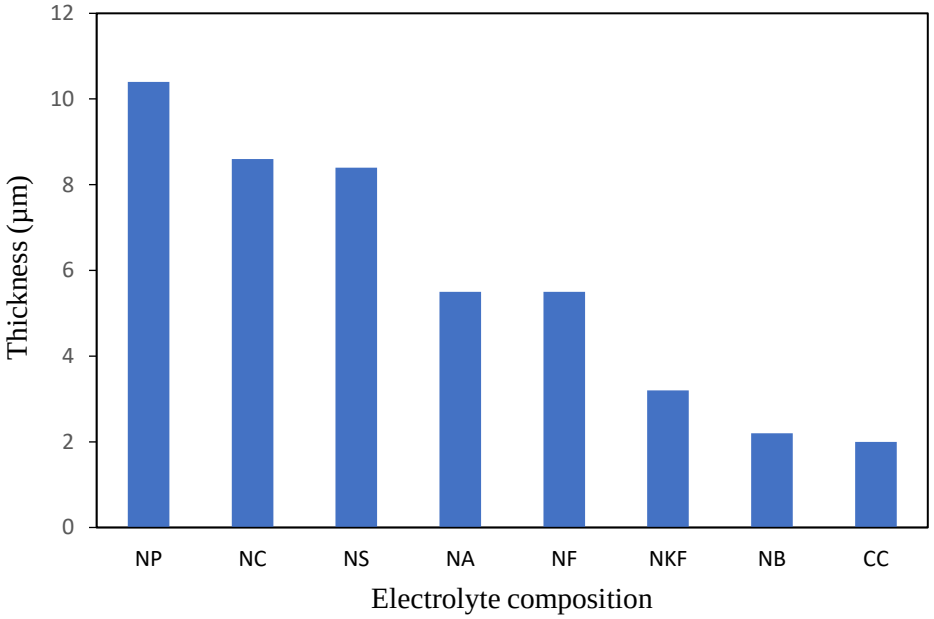

Figure 2.11 Thickness of the formed PEO layer in different electrolytes [14, 23].

It is shown addition of alumina particles to the electrolyte can enhance the adhesive wear properties of commercially pure titanium under pulsed DC regime [88]. Increase in concentrations of hard alumina nanoparticles result in higher level of agglomeration and thus a lower wear mass loss rates of the coatings.

Two step PEO has also been employed to improve surface coating properties of titanium alloys [4]. First, titanium oxide is formed on Ti–15V–3Al–3Cr–3Sn in alkaline aluminate electrolyte in order to enhance the wear resistance of titanium alloy. The coating possesses high wear resistance, but coating adhesion to substrate due to the formation of a number of voids and pores in the oxide layer close to the

substrate was not good. In order to improve coating adhesion second step process was conducted in acid sulfuric and acid phosphoric. In this step voids and pores are filled with an oxide produced in acidic solutions. Applying the second step, not only decrease the high wear resistance of coating, but also increase the adhesion of coating. All of these studies provide useful information about the coating properties produced in different electrolytes. However, the underlying reason of these differences in properties were not fully explained.

2.5.2 Current Mode

The type of applied current mode can also affect the intensity and density of discharges during PEO [17, 87, 89]. As has been previously mentioned, most of the reactions take place in discharge channels and affect the coating microstructure and composition [61]. DC current mode develops long lasting micro discharges; therefore, it is suitable to study the microdischarge characteristics and mechanism of PEO. However, controlling the process is harder under this condition.

Pulsed DC current mode gives us this opportunity to have more control over the process. By applying regular interruptions and changing the discharge size and intensity, using frequency and duty cycle of the pulses, coatings with enhanced

properties can be produced [13, 90]. Energy of each pulse (E_p) can be calculated using the equation [91].

$$E_p = \int_0^{ton} Vp.Ip\ dt \qquad (2.1)$$

where V_p is the voltage of the pulse, I_p is the pulse signal, and dt is the duration of each pulse when it is on. By changing the pulse parameters such as voltage, current, frequency, and duty cycle, plasma discharge characteristics can be changed and affect the coating properties. Dehnavi et al. studied the effect of frequency and duty cycle on microdischarge behavior during plasma processing by applying pulsed DC current mode on 6061 aluminum alloy [28]. PEO coatings were created at different power frequencies of 50, 500, 1000 and 2000 Hz and duty cycles of 10%, 20%, 50%, and 80% at constant current. Applying low duty cycles produced large number of soft microdischarges which resulted in higher coating growth rate at constant current, Figure 2.12. It was shown that by increasing the duty cycle, microdischarges became stronger but their spatial density decreased.

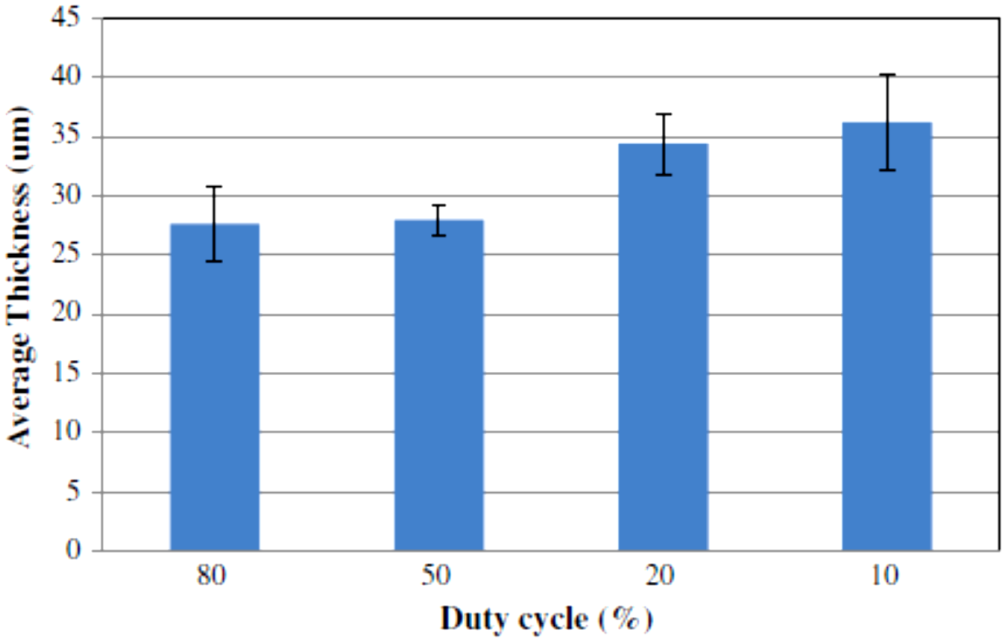

Figure 2.12 Effect of duty cycle on coating thickness on samples coated at 1000 Hz [28].

Use of the AC current mode removes the additional electrode polarization and improves the control over the process by interrupting microdischarges. However, using only one frequency and limitation in reaching high powers are drawbacks which inhibit commercialization of this mode [87].

As it was shown, most of the studies that have been performed so far focus on the effect of electrolyte, current mode, time, etc. to enhance coating properties without having a holistic understanding of the entire process and key variables.

Understanding the PEO mechanism provides unique opportunity to fully utilize the potentials of this process in many applications and for various systems, especially low density reactive metals and alloys based on Ti, Al, and Mg.

Chapter 3

Experimental Methods

3.1 Materials

Rectangular samples of CP Ti with dimensions of 25 mm×20 mm×0.5 mm were used as the substrate material. Prior to PEO surface treatment, the samples were polished with emery papers and alumina powder to achieve an average mean surface roughness of R_a = 0.1 µm following by cleaning with acetone and deionized water.

3.2 Plasma Electrolytic Oxidation Setup

The coatings were prepared in a stable alkaline electrolyte containing 0.01 M $K_4P_2O_7$ and 0.02 M KOH at pH= 12 with a conductivity of 7.1 mS/cm. During the oxidation process, the electrolyte was stirred in an 800 mL double walled beaker with water coolant flow to keep the electrolyte temperature below 30 °C. The samples were secured to an externally insulated metallic rod and suspended in the center of the electrolytic cell as the anode, surrounded by a cylindrical stainless-steel plate cathode, Figure 3.1.

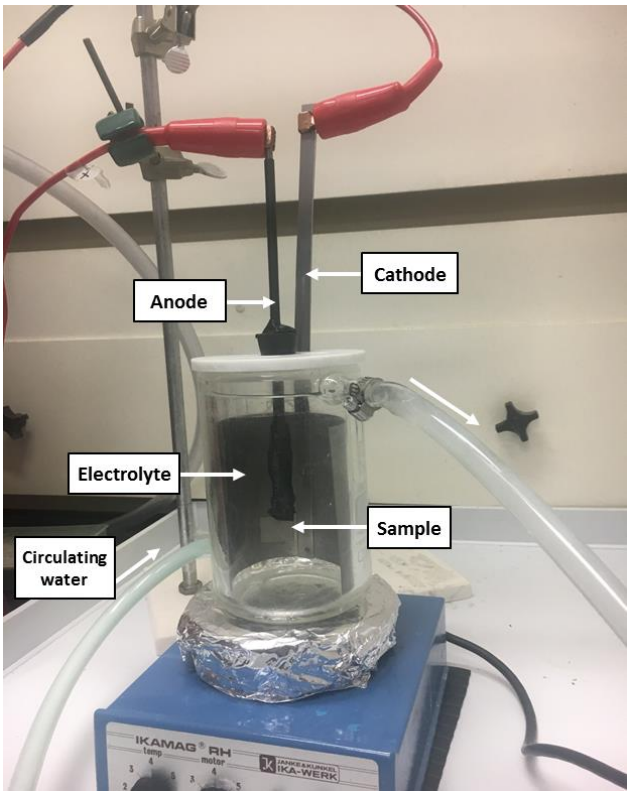

Figure 3.1 PEO reactor and setup.

The treatments were performed at different current densities, i.e., 30, 40, 50, 60, 80, 100, and 120 mA/cm^2 using a 10 kW power supply (Sorenson model SGA-3u). Initially, the voltage was increased to the desirable current density and then controlled to maintain that level. The treatments were continued until intense arcing was observed, in order to avoid the detrimental effects of these arcs on the coating. During the PEO treatment, voltage and current were recorded continuously using a Tektronix oscilloscope.

3.3 Characterization Methods

3.3.1 X-ray Diffraction (XRD)

XRD was used to identify the crystalline phases present in the PEO coatings by scanning in the 2θ = 20–80◦ range (Bruker D8 Advance X-ray diffractometer). Radiation was emitted from a Cu Kα source with a wavelength of 1.54 Å and accelerating current and voltage of 40 kV and 40 mA, respectively. A scan speed of 3 sec/step and increment of 0.01° was utilized in order to get accurate results. XRD scan were conducted in θ-2θ mode for all the coatings and in low angle mode for selected current densities.

3.3.2 Scanning Electron Microscopy (SEM) and Energy Dispersive X-ray Spectroscopy (EDS)

The surface morphology of the coatings was examined using Hitachi S-3000N SEM. All SEM micrographs were taken using an accelerating voltage of 30 keV and a typical working distance of 15 mm. SEM was used to examine the cross-sectional morphology of selected samples and measure the coating thickness in order to find the growth rate. EDS was utilized for elemental mapping and analysis of the coatings. Also, focused ion beam (FIB) was used to examine the cross-sectional morphology of selected samples. Quantitative studies of coating porosity were performed using an image analysis software (ImageJ).

3.3.3 Optical Profilometry

White Light Interferometry (Bruker NPFLEX) studies were conducted to evaluate the surface topography and roughness. A 10X objective lens was utilized to measure roughness and surface indices. R_a and surface index values were utilized to study the surface profile of the samples. R_a is the arithmetic average of all surface heights in the sample shown in Equation 3.1, and surface index is the ratio of actual surface area to the nominal area.

$$R_a = \frac{1}{n}\sum_{i=1}^{n}|y_i| \tag{3.1}$$

3.3.4 Transmission Electron Microscopy (TEM)

The microstructure of the coatings was studied by TEM. Cross-sectional TEM specimens were prepared by the procedure of mechanical grinding, polishing, dimpling and Ar-ion milling. Selected-area electron diffraction (SAED) patterns and high-resolution (HR) TEM images were recorded in a Hitachi H-9500 electron microscope with an accelerated voltage and point to point resolution of 300 kV and 0.18 nm, respectively. Moreover, ImageJ software was employed to measure the crystalline area of the coatings in TEM micrographs.

3.3.5 X-ray Photoelectron Spectroscopy (XPS)

The surface composition and chemical state of the elements in the coatings was determined by XPS. XPS surface analysis was performed with a Perkin-Elmer spectrometer using an Al Kα monochromatic x-ray source (1484.6 eV). The pressure was maintained below 10^{-9} Torr. The XPS spectra of the coatings were calibrated using the C 1s peak at a binding energy of 284.5 eV. High resolution spectra for each element were obtained at 50 eV pass energy taken in increments of 0.2 eV with dwell time of 100 ms for at least 200 scans. The CasaXPS software was used for XPS spectra deconvolution.

Chapter 4

Results and Discussion

4.1 Plasma Electrolytic Oxidation

4.1.1 Voltage- Time Response

Figure 4.1 shows the V-t response as a function of current density. The anodic process occurs in three distinct phases, easily discerned from the V-t graph. During the initial stage (up to breakdown voltage), the voltage increases linearly with time and the process is accompanied by the evolution of gaseous oxygen on the anodic surface due to the electrolysis of water. In this region, no apparent sparks are found on the metal surface and the total current is represented by the ionic current due to the diffusion of electrolyte ions. According to Faraday's law, the ionic current plays the main role in forming the oxide [15, 92, 93].

In the second stage (up to the critical voltage), the system begins to deviate from the previously observed linearity and the slope of the V–t curves is decreased. Due to the high electric field, dielectric breakdown (electron avalanche) occurs and a large number of small size sparks is uniformly distributed over the whole surface in this stage. Once the sparking occurs, the current density is represented by the sum of the ionic current and the electron current caused by the sparking. A

relatively lower rate of voltage increase is needed to maintain the same current value compared to the first region since the electron current density is mainly due to sparking and as such is independent of the coating resistance.

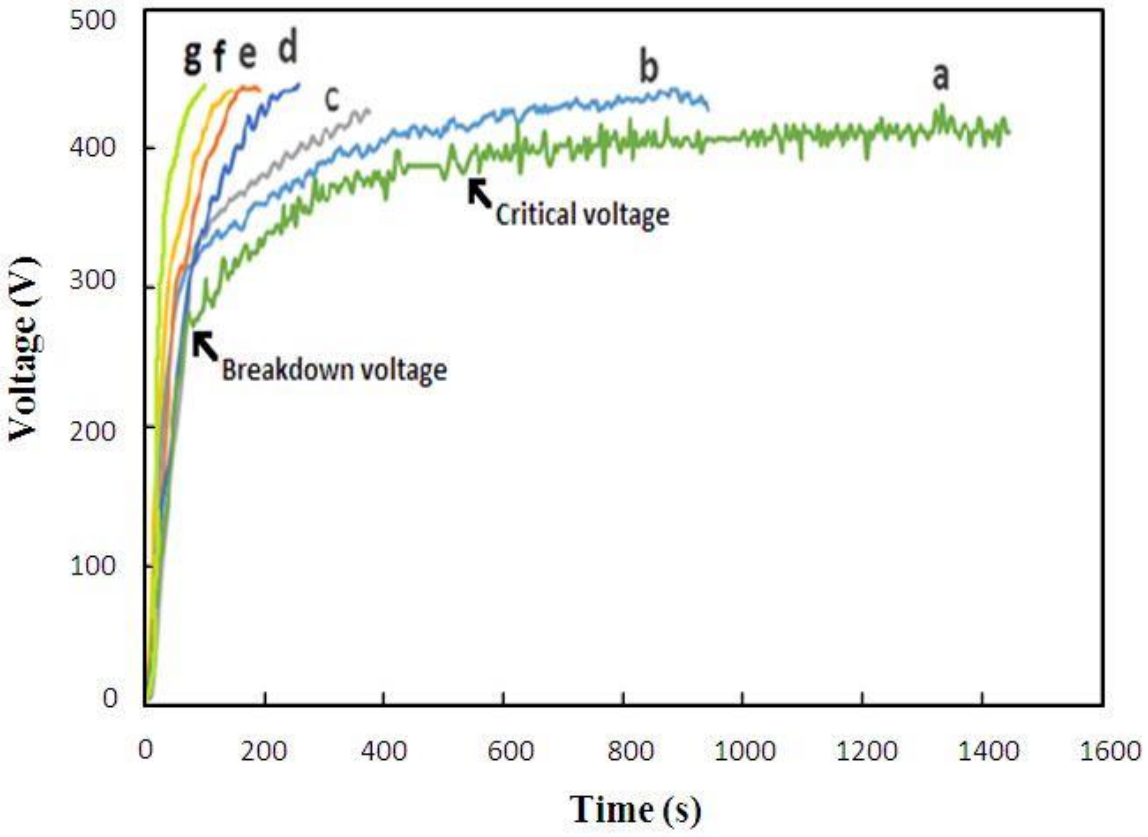

Figure 4.1 Voltage vs. time plots obtained during PEO at current densities of (a) 30 (b) 40 (c) 50 (d) 60 (e) 80 (f) 100 (g) 120 mA/ cm^2.

In stage III, the anodic voltage, attains a relatively stable value indicating that the coating has reached a constant resistance configuration and no major increase in the anodic voltage is needed to maintain the same current. The slope change in this stage may be attributed to the significant increase in the fraction of the electronic current in the total current associated with the dielectric breakdown.

Figure 4.1 shows that processing time before arc initiation decreases as the applied current density increases. At 30 and 40 mA/cm^2, long processing times can be obtained and all three stages of the coating formation are visible. At these two current densities, the electronic current is dominant. At current densities higher than 40 mA/cm^2, the third stage is not present. As can be seen, by increasing the current density both, the slope of the V-t curve and the fraction of the ionic to total current increase. At 100 and 120 mA/cm^2, the voltage increases almost linearly with time maintaining a sharp slope. At these higher values, the current density exhibits only the first stage of coating growth and the total current is mostly equal to ionic current.

4.1.2 Total Charge Considerations

Figure 4.2 shows the variation of total charge (I×t) vs. the applied current density. As discussed earlier, the time refers to the time just before the onset of arcing. At 30 mA/cm^2, the charge density exhibits a maximum value and a high

density of sparks is observed on the sample surface. The decrease in the charge density at higher current density values can be due to the decrease in the contribution of the electronic current to the total current. From 60 mA/cm^2 to 100 mA/cm^2, the charge density exhibited a plateau indicating a balance between the electronic and ionic current. For 120 mA/cm^2 arcs are more intense and the charge density is lower compare to other conditions.

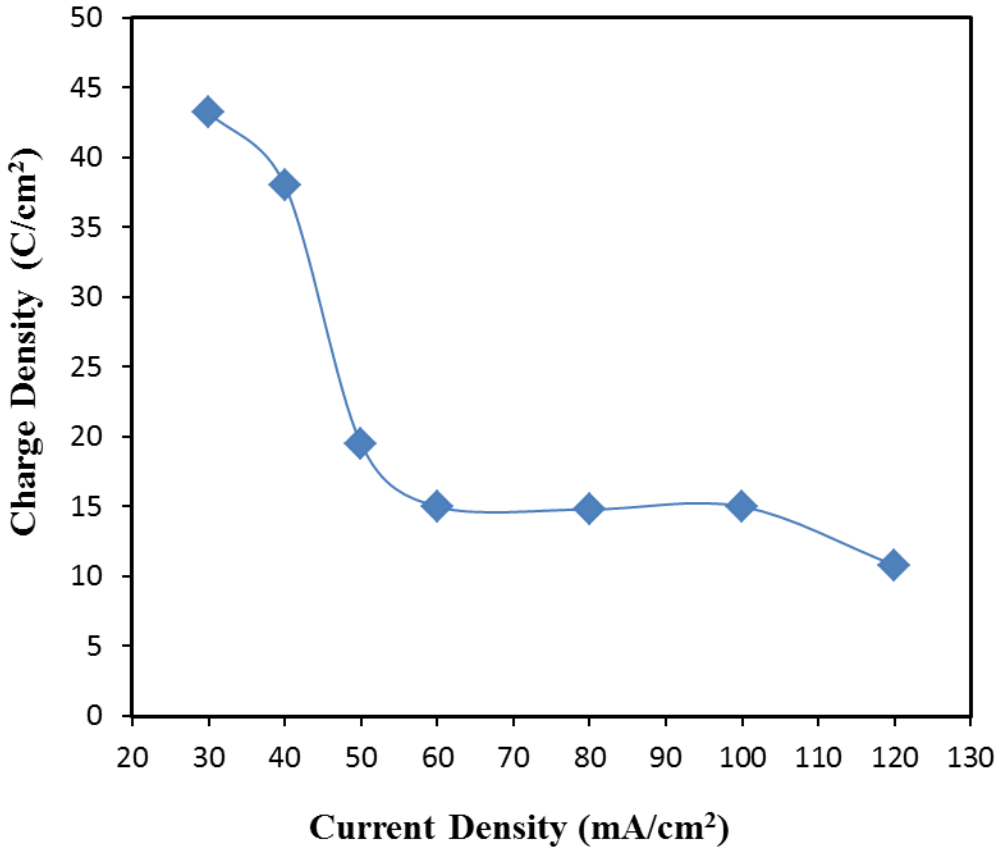

Figure 4.2 Charge density vs. current density plot obtained during PEO processing.

4.1.3 Incorporation Rate of Ionic/Electronic Charge

The effective ionic charge can be obtained by measuring the average coating thickness using cross-sectional SEM micrographs. First, the mass of the produced coating was found, using the measured volume and density of the titanium oxide. Then, by applying the Faraday's law, the effective ionic charge is determined, Equation 4.1 [94].

The various parameters in this equation are: m coating mass (g), *Q* the effective ionic charge, *F* the Faraday constant (96485 C mol^{-1}), *M* the molar mass of the substance (g/mol), and *z* the valence number of ions of the substance (electrons transferred per ion).

$$m = \left(\frac{Q}{F}\right)\left(\frac{M}{Z}\right) \qquad (4.1)$$

For titanium oxide, the parameter values are:

- M= 79.88 (gr/mol)
- ρ= 4.23 (gr/cm^3)
- Z = 4 for this reaction $Ti^{4+} + 2O^{2-} \longrightarrow TiO_2$

Also, the total applied charge composed of ionic charge (caused by diffusion of ions) and electronic charge (caused by sparking) passed through the substance (coulombs) was found in previous part, Figure 4.2.

Although discharge channels developed by sparking facilitate the reaction, oxide formation is mainly the result of ionic current [95]. Therefore, the incorporation rate of the effective ionic charge, was roughly determined by calculating the ratio of the effective ionic charge, to the total charge. The remaining part is considered to be the electronic charge contribution, Figure 4.3. The results show that by increasing the current density, the incorporation rate of ionic charge increases, while that of the electronic charge decreases.

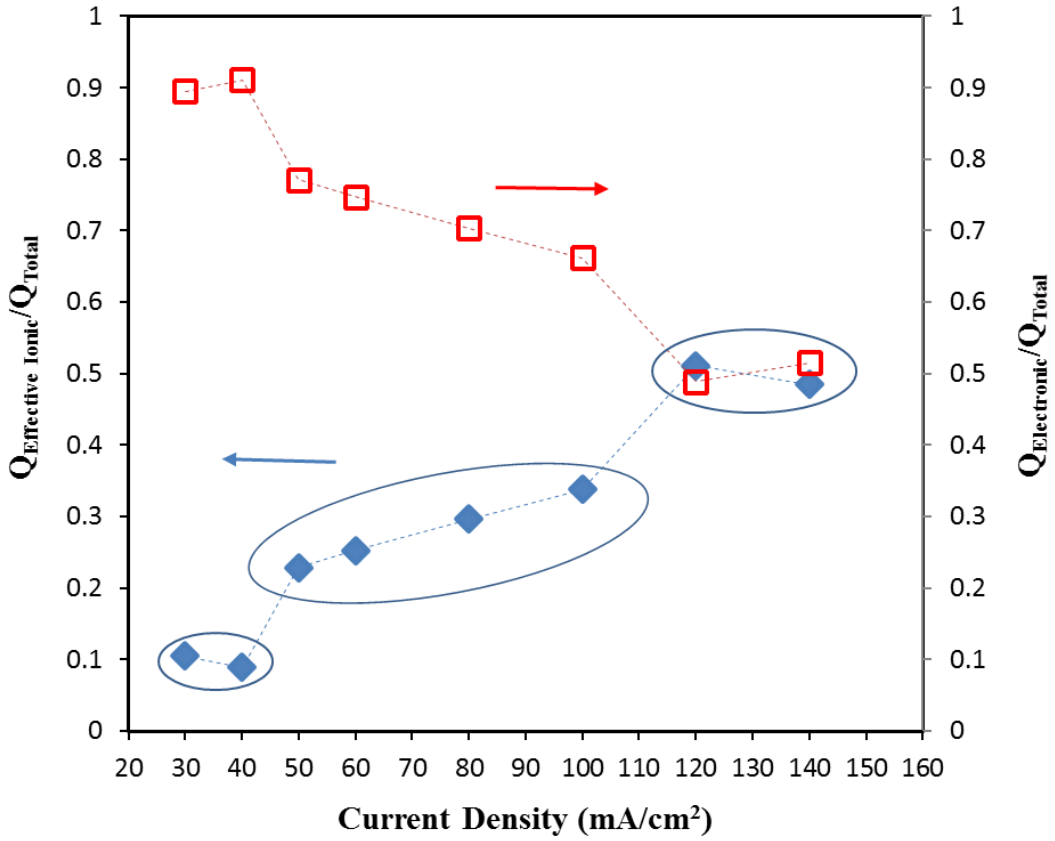

Figure 4.3 Ionic and electronic current incorporation rate at different current densities.

Furthermore, the results show three interesting stages of behavior. In the first stage, for coatings processed at low charge densities (30 and 40 mA/cm^2), the contribution of ionic charge is very small. This means that a large number of discharge channels develop in the oxide, but there are not enough ions to diffuse through them and react. In the second case, for the coatings processed at

intermediate values (50 to 100 mA/cm^2), the incorporation rate of ionic charge increases, but there is a moderate number of ions for oxide formation and the contribution of electronic charge is still higher. In the third case, for the coating processed at high charge densities (120 and 140 mA/cm^2) equal amounts of ionic and electronic charge prevail. This case results in the highest growth rate (Table 4.3) presenting an optimum balance of ionic and electronic charges. It clearly shows a complementary action between available ions and discharge channels. Thus, in order to achieve high growth rates, equal or balanced contributions from ionic (diffusion of ions for reaction) and electronic (generation of channels) charges are required.

4.2 Characterization

4.2.1 Surface Topography Analysis

Figure 4.4 illustrates the surface topography of the produced layers on CP Ti processed at selected current densities. As can be seen, the coating surfaces become smoother as the current density increases. In order to obtain a better understanding of the topography, the average roughness (R_a) and surface index (ratio of actual surface area/nominal area) are presented in Table 4.1. The results showed a general trend indicating that decreasing the current density led to an increase in average

roughness, surface index and porosity. Due to the major contribution of the electronic current at low current densities, a high number of micro discharges forms increasing the porosity and surface roughness. It is interesting to note that the samples processed from 60 to 100 mA/cm^2 form a plateau in the charge vs current density curve, and show rather similar characteristics in terms of roughness and surface index. Moving to the highest current density, some deterioration of surface occurs as reflected in the roughness and surface index. It is interesting to note that, as the current density increases, the porosity decreases, due to the higher incorporation rate of ionic current and sealing effect on the pores.

Table 4.1. Charge density, average roughness, surface index, and porosity of the PEO coatings at different current densities.

Current Density (mA/cm^2)	30	40	50	60	80	100	120
Charge Density (C/cm^2)	43.4	38	19.5	15	14.8	15.2	10.8
Average Roughness (R_a)	2.0	1.6	1.5	1.4	1.4	1.3	1.5
Surface Index	7.1	6.8	5.5	3.5	3.6	3.9	5.5
Porosity %	20.1	15.2	13.3	12.8	11.9	8.2	7.9

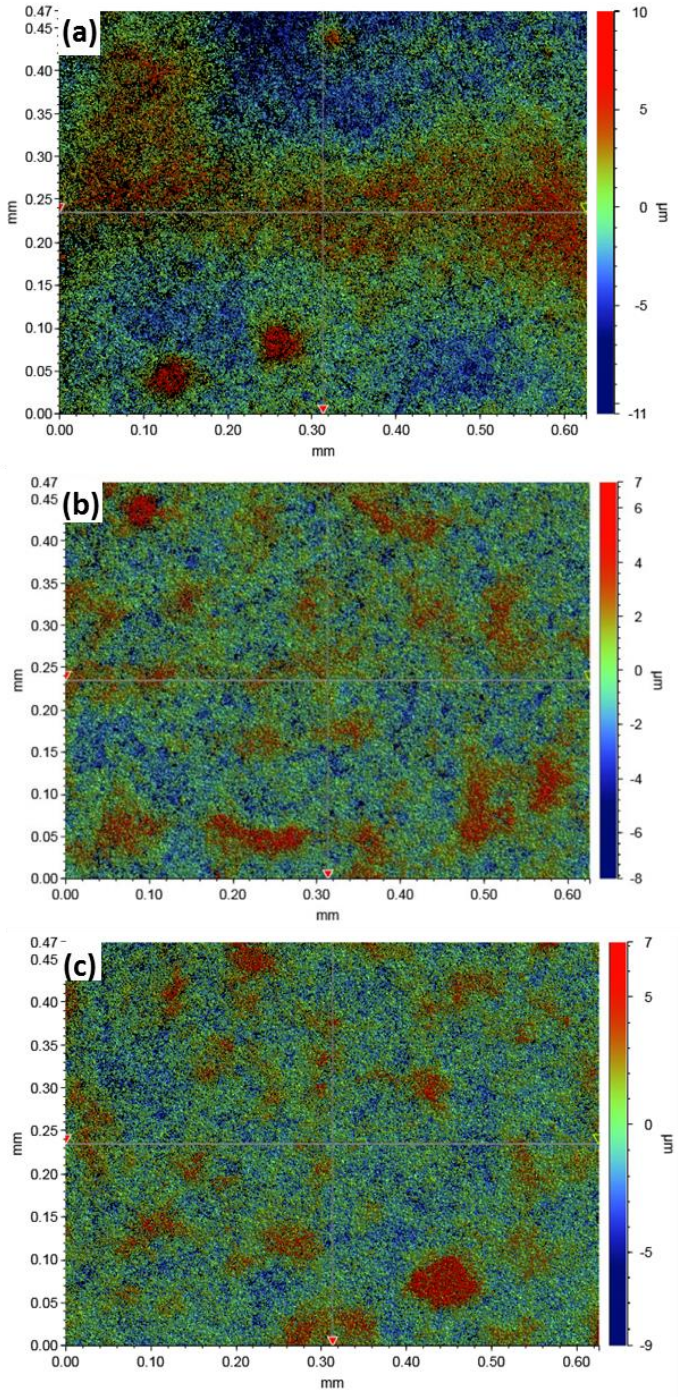

Figure 4.4 Surface profile using white light interferometry of the PEO-coated sample at current densities of (a) 30, (b) 80 and (c) 120 mA/cm^2.

4.2.2 XRD Studies

Figure 4.5 presents the XRD patterns from the PEO produced layers at various current densities. The peaks (marked by "Δ") at 2θ angles of 25.25°, 48.06°, and 62.68° have a lattice spacing of 3.52 Å, 1.89 Å, and 1.48 Å and can be identified, respectively, the (101) and (200) and (204) planes of the anatase TiO_2 structure.

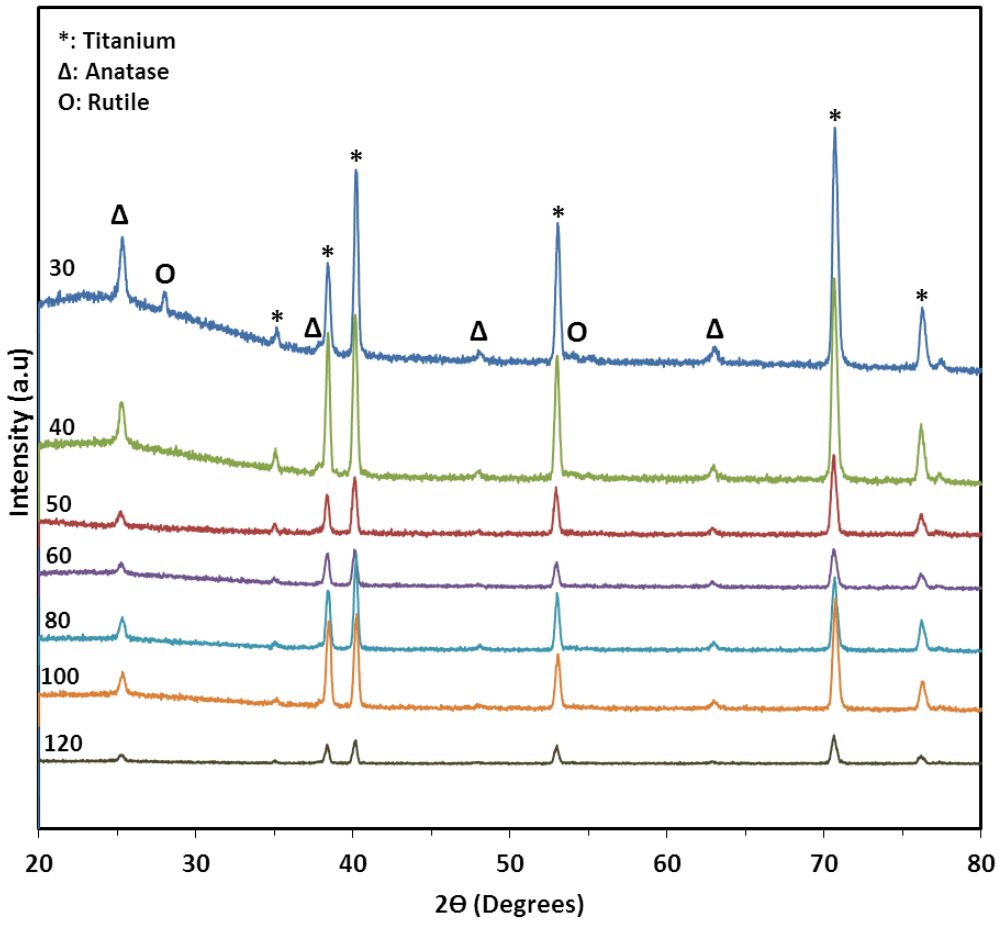

Figure 4.5 XRD patterns of the coatings formed at different current densities.

The peaks (marked by “O”) at 2θ angles of 27.8° and 54.36° have a lattice spacing of 3.25 Å and 1.68 Å corresponding to the (110) and (211) planes of the rutile TiO_2, respectively. The peaks (marked by “*”) are diffraction peaks of the Ti substrate. The XRD results indicate that anatase TiO_2 was formed in all coatings, while rutile TiO_2 was only formed in the coating produced at lower current densities. At low current densities, the contribution of electronic current is higher, and results in the development of a greater number of plasma discharges. These microdischarges provide enough energy and raise the temperature required for rutile formation. Additionally, sufficient time favored the anion diffusion and time dependent transformation of metastable anatase to thermodynamically stable rutile phase. On the contrary, the samples processed at higher current densities, showed lower density of plasma discharges and produced only the anatase phase. These results are in agreement with ART findings which discussed earlier [47].

The broad peak around 2Θ=20-35° observed mainly in samples processed at low current densities and is attributed to the formation of an amorphous phase. This was favorable to be a P containing phase that is discussed in a later section. As the crystallite size becomes smaller, the XRD peak becomes broader and amorphous phase can be considered as the accumulation of low order crystalline phases

4.2.3 Surface Morphology Analysis

Figure 4.6 presents SEM images of the coated layers obtained at selected PEO current densities. It is clear that the surface produced at lower current densities (higher charge density), Figure 4.6(a), shows a large number of fine pores compared to samples processed at 80 and 120 mA/cm^2 shown in Figure 4.6 (b) and (c), respectively. This surface appearance is consistent with the observed R_a and the role of the ionic and electronic current discussed above. Porosity percentage of different coatings is presented in Table 4.1. Moreover, pore size distribution of the coatings produced at these current densities is presented in Figure 4.7. It is shown that as current density increases, the number of small pores (<0.6 μm) increased. However, the density of larger pores (> 0.6 μm) decreased.

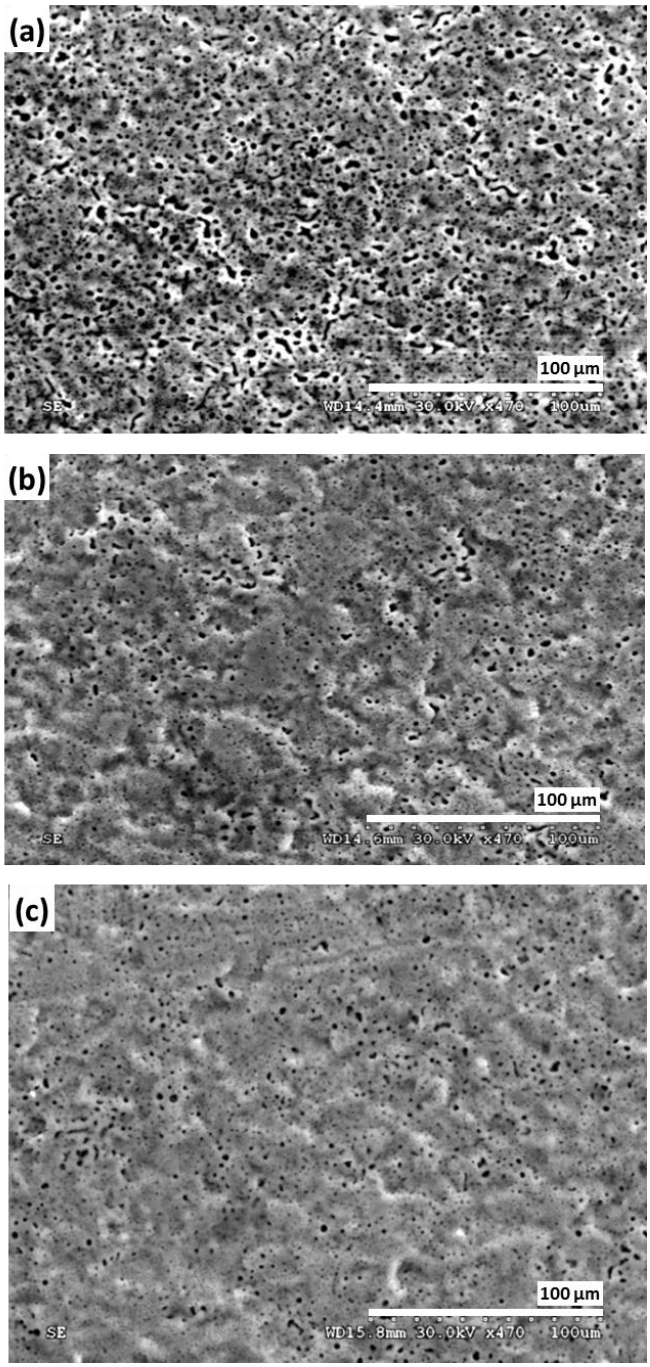

Figure 4.6 SEM images showing surface morphology of PEO coated samples at current densities of (a) 30, (b) 80, (c) 120 mA/cm^2.

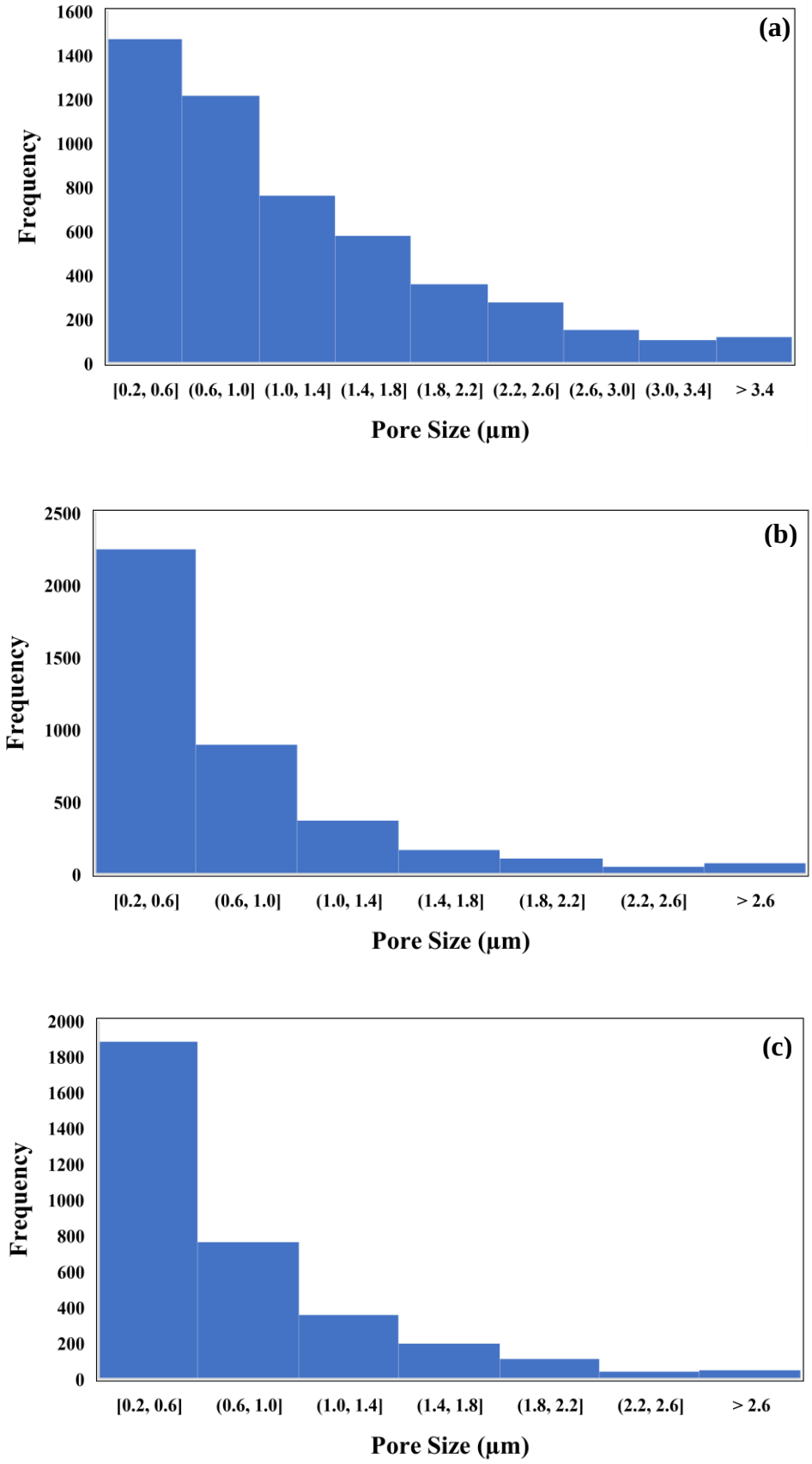

Figure 4.7 Pore size distribution of coated samples processed at current densities of (a) 30, (b) 80, (c) 120 mA/cm^2.

Figure 4.8 shows a typical EDS spectrum from a PEO coating surface. The amounts of Ti, O and P were similar for all surfaces, as shown in Table 4.2. These results show that the PEO processing condition has no major effect on the coating chemistry.

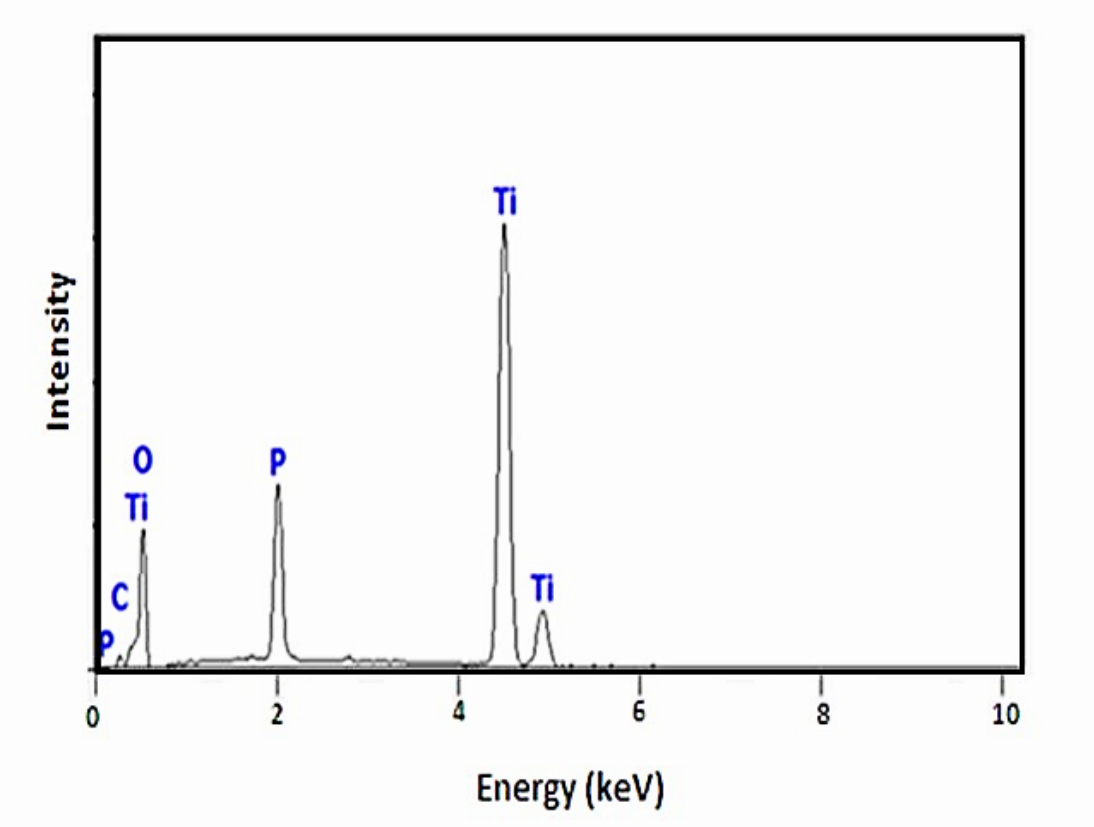

Figure 4.8 Typical EDS spectrum from the surface of a PEO coated samples.

Table 4.2 Elemental compositions of coatings at different current densities obtained by EDS.

Current density (mA/cm^2)	Ti (at%)	O (at%)	P (at%)
30	30.8	62.0	7.1
40	32.9	59.4	7.6
50	31.7	61.2	7.1
60	29.8	62.3	7.8
80	34.2	57.1	8.7
100	29.9	62.3	7.8
120	34.4	56.9	8.7

Figure 4.9 presents SEM and corresponding EDS maps of titanium (Ti), oxygen (O), and phosphorous (P) of a pore on the coating surface processed at 120 mA/cm^2. As it shown, titanium and some amount of phosphorous are present inside the pore, however, no oxygen is detected. Thus, this provides some indications that the pore might be extended to the titanium substrate. It can be suggested that after generation of the microdischarge event, this discharge channel did not fill with oxide completely and left behind a hollow pore.

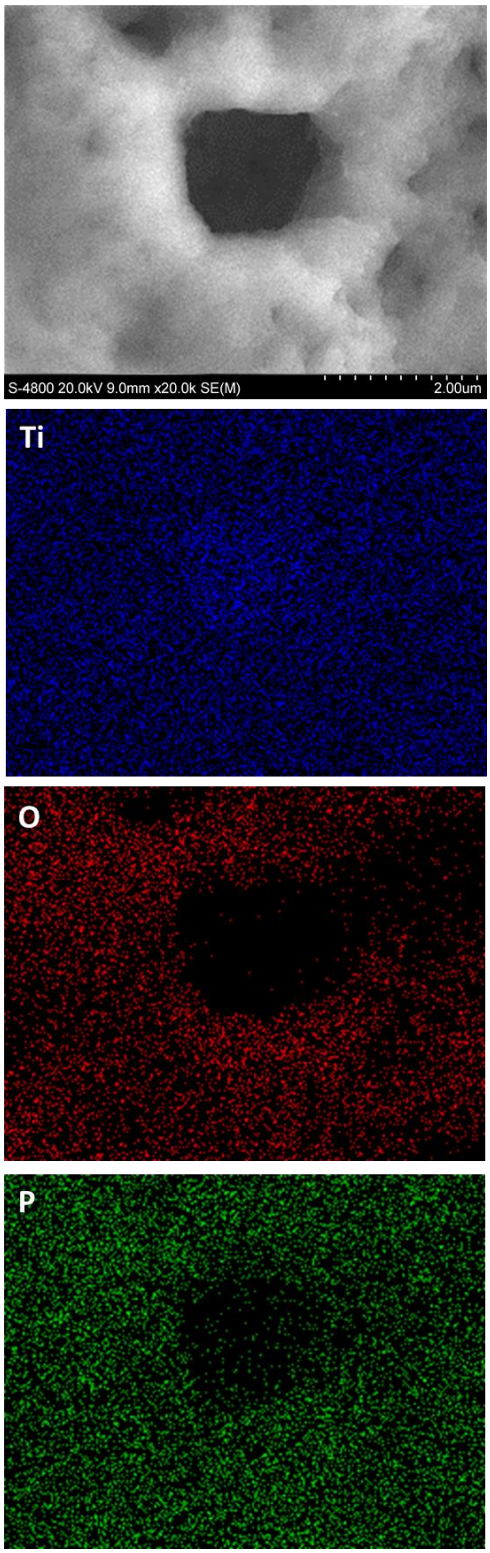

Figure 4.9 SEM of the coated sample processed at 120 mA/ cm^2 and Ti, O, and P elemental maps.

Figures 4.10 (a), (b), and (c) are cross-sectional SEM images of three PEO coatings prepared using current densities of 30, 80 and 120 mA/cm^2. Coating thickness is almost the same for all the coatings. However, the growth rate increases sharply with increasing the current density due to the higher incorporation rate of ionic current (Table 4.3). It is noted that for lower current densities, pores exist at both the metal/oxide interface and throughout the coating which is in agreement with the surface morphology observations, Figure 4.6. Titanium oxide is considered to be an oxygen deficient n- type semiconductor [95, 96]. In this oxide, O^{2-} migrated inward with transport number of ~0.4 and Ti^{4+} cations move outward with transport number of ~0.6 [95]. Thus, TiO_2 is expected to grow faster inward to the substrate than in the outward direction [97]. Presence of some fine pores on the coating surface and in coating/substrate interface, can be attributed to the outward migration of Ti^{4+} ions and lack of time for filling all the discharge channels during the process. The X-ray map in Figure 4.11 provide some evidence for this type of growth.

It is shown that the coating prepared with a smaller current density, i.e., 30 mA/cm^2, have a smoother interface between the coating and Ti substrate, compared to that prepared with a higher current density, i.e. 120 mA/cm^2. In other word, increasing the current density during the coating preparation increase the roughness of the interface between the coating and Ti substrate. This can be attributed to the diffusion of large number of ions with high energy at higher current densities.

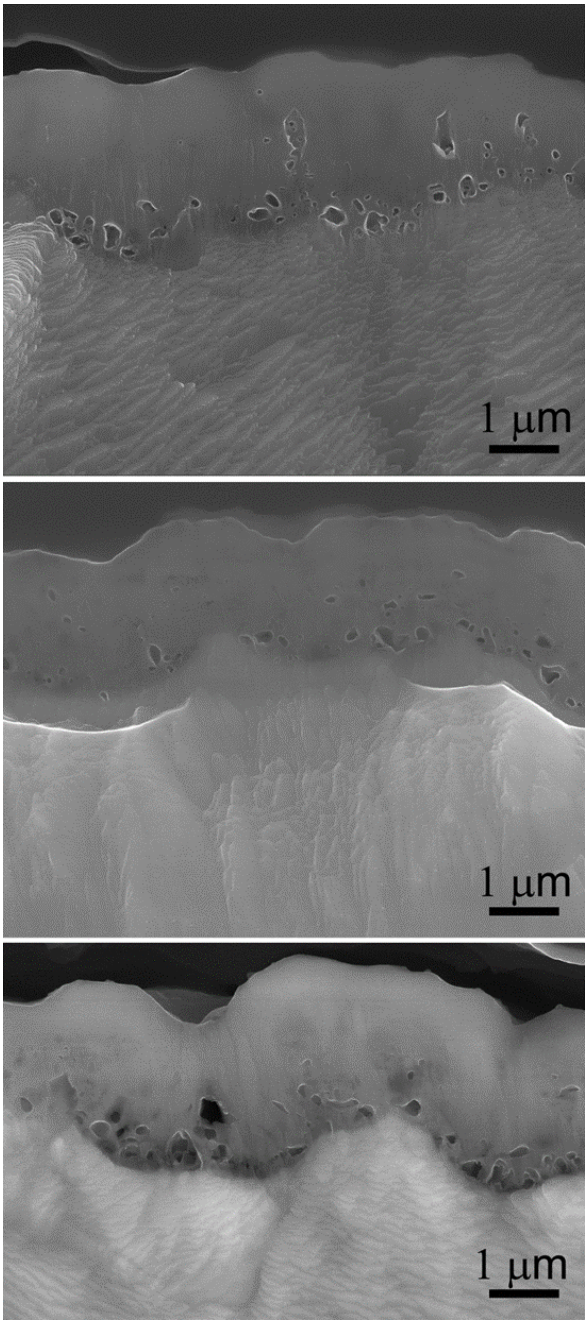

Figure 4.10 Cross-section SEM images of the coatings prepared using current densities of (a) 30, (b) 80, (c) 120 mA/cm^2.

Table 4.3 Thickness and growth rate of the coatings processed at different current densities.

Current Density (mA/cm^2)	30	40	50	60	80	100	120
Thickness (μm)	2.3	1.7	2.4	1.9	2.2	2.6	2.7
Growth Rate (nm/s)	1.6	1.8	6.1	7.6	11.9	17.1	30.0

Figure 4.11 shows SEM micrographs and EDS elemental maps of the cross sections of the coatings for samples processed at 30 mA/cm^2 and 120 mA/cm^2. No significant difference can be detected in distribution of titanium and phosphorous for these coatings. However, distribution of oxygen is different for these samples. At 30 mA/cm^2 oxygen is distributed more evenly throughout the coating, whereas at 120 mA/cm^2 high concentration of oxygen is detected at the bottom of the oxide layer.

The distribution of the oxygen in the coatings could be attributed to the incorporation rate of ionic and electronic current at different current densities. At low current densities, the electronic current contribution is more and large number of plasma discharges are produced during the PEO process which is evident in SEM micrographs of the coating surface, Figure 4.6. This phenomenon, results in formation of more discharge channels for oxygen ions to diffuse through in different areas and distribution of oxygen within the coating would be uniform.

However, at higher currents, ionic current incorporation rate is high and oxygen ions have enough energy to diffuse in the oxide and reach the bottom layer of the coating. High concentration of oxygen at the bottom layer, can assist the formation of crystalline titanium oxide in that part of the layer which is discussed later in TEM section.

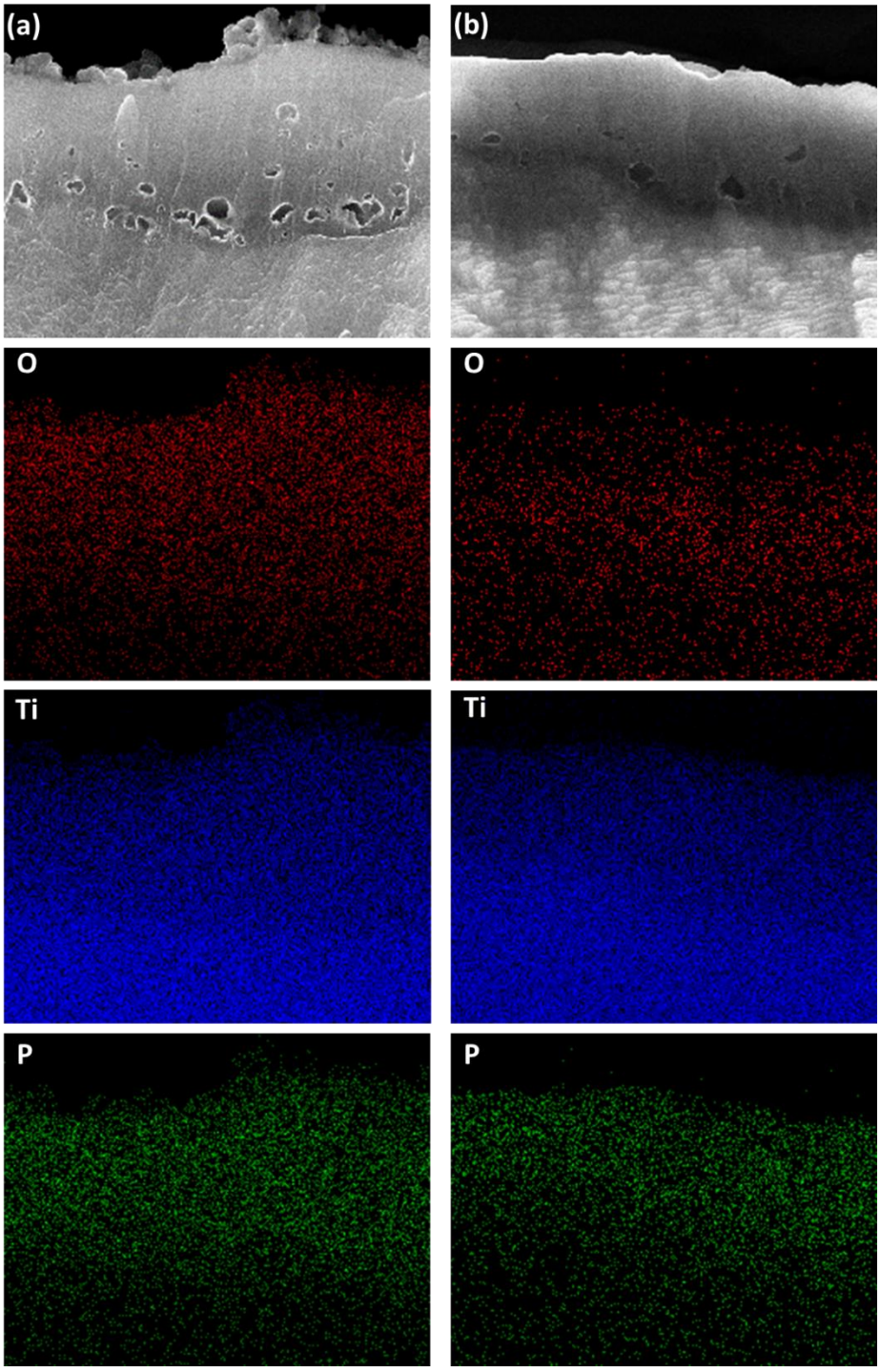

Figure 4.11 Left side: (a) SEM of the coated sample produced at 30 mA/cm^2 and O, Ti, and P elemental maps; Right side: (b) SEM of the coated sample produced at 120 mA/ cm^2 and corresponding O, Ti, and P elemental maps.

4.2.4 TEM Studies

TEM studies have been employed to systematically study the microstructure of the selected representative coatings and the influence of the current density on the coating microstructure. Figures 4.12 (a), (b) and (c) show cross-section TEM images of the coatings prepared using current densities of 30, 80 and 120 mA/cm^2, respectively. The micrographs show the entire microstructure of each entire coating from the coating/Ti interface to the top surface. All three coatings are basically composed of two layers: an amorphous layer on the top and a composite layer close to the substrate. The amorphous layer on the top is dense and homogenous without porous structure while the bottom composite layer has a complex microstructure consisting of nanocrystalline structure, amorphous structure and nano pores. An amorphous phase forms at the coating/electrolyte interface. It is suggested that constant cooling of the electrolyte and low thermal conductivity of the oxide may inhibit the top layer of the coating from overcoming the required crystalline titanium oxide activation energy forming a crystalline phase.

The thickness of the bottom complex layer in general increases with the current density for the coating preparation, whereas the thickness of the top amorphous layer is not strongly affected by the current density. This is consistent with the argument that quenching by the electrolyte produces the amorphous layer. The average thickness of the top amorphous layer in three coatings is around ~700-800

nm. In other words, the thickness ratio between the bottom complex layer and the top amorphous layer increases by increasing the applied current density. The crystalline phase area of the samples was measured by ImageJ software using TEM micrographs. The percentage of crystalline area for the samples processed at 30, 80, and 120 mA/cm^2 is 18%, 56%, and 64%, respectively. Increasing the portion of the crystalline phase in the coating by increasing the current density can be attributed to the higher incorporation rate of ionic current.

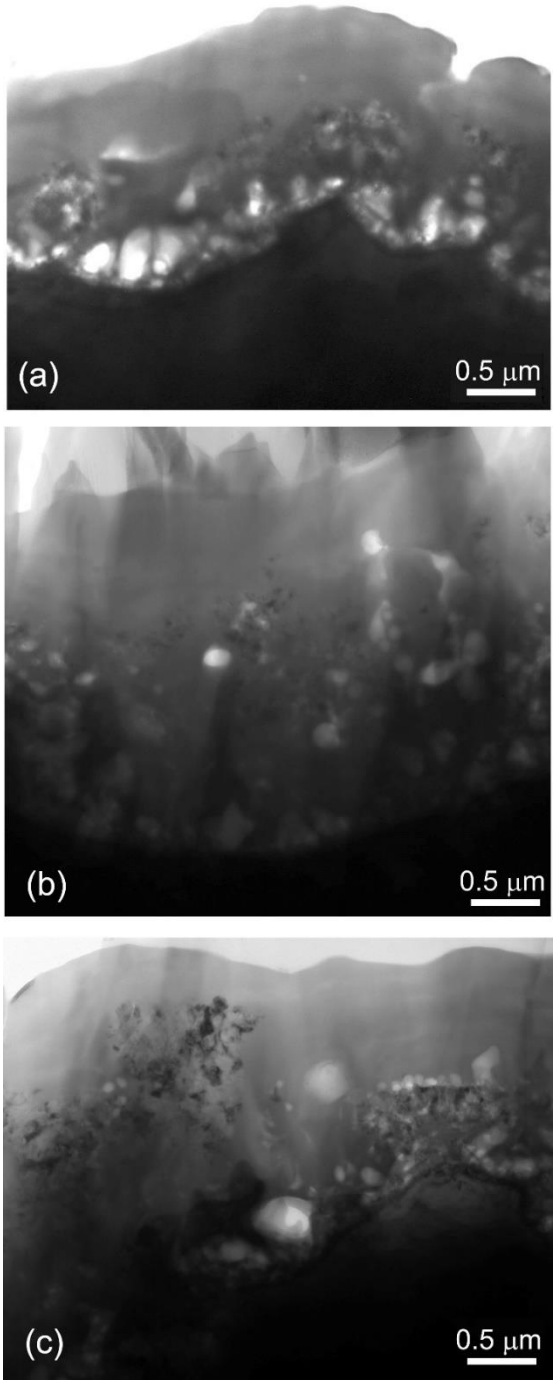

Figure 4.12 Cross-section TEM images of the coatings prepared using current densities of (a) 30, (b) 80, (c) 120 mA/ cm^2.

Figure 4.13 (a) is a zoom-in cross-section TEM image for the coating prepared using a current density of 30 mA/cm^2 showing a detailed microstructure of the entire coating. This layer basically consists of four sublayers which can be characterized in the sequence starting from the one at the interface with the substrate: (1) a dense fine nanocrystalline sublayer with a thickness of ~70 nm (SL I), (2) a sublayer of a high density nano pores (SL II), (3) a sublayer with a majority of amorphous structure and a small number of nano pores (SL III); (4) a sublayer consisting of coarse nanocrystalline (SL IV). The crystalline size in SL I is ~7-10 nm, whereas that in SL IV is ~8 - 25 nm. The interface between the coating and Ti substrate is consisting of peak and valley regions. The thickness of SL I and SL II usually remains consistent regardless of the morphology of the interface. After examining several regions of the coating structure, it was found that the thickness of SL III and SL IV is not consistent along the coating/substrate interface.

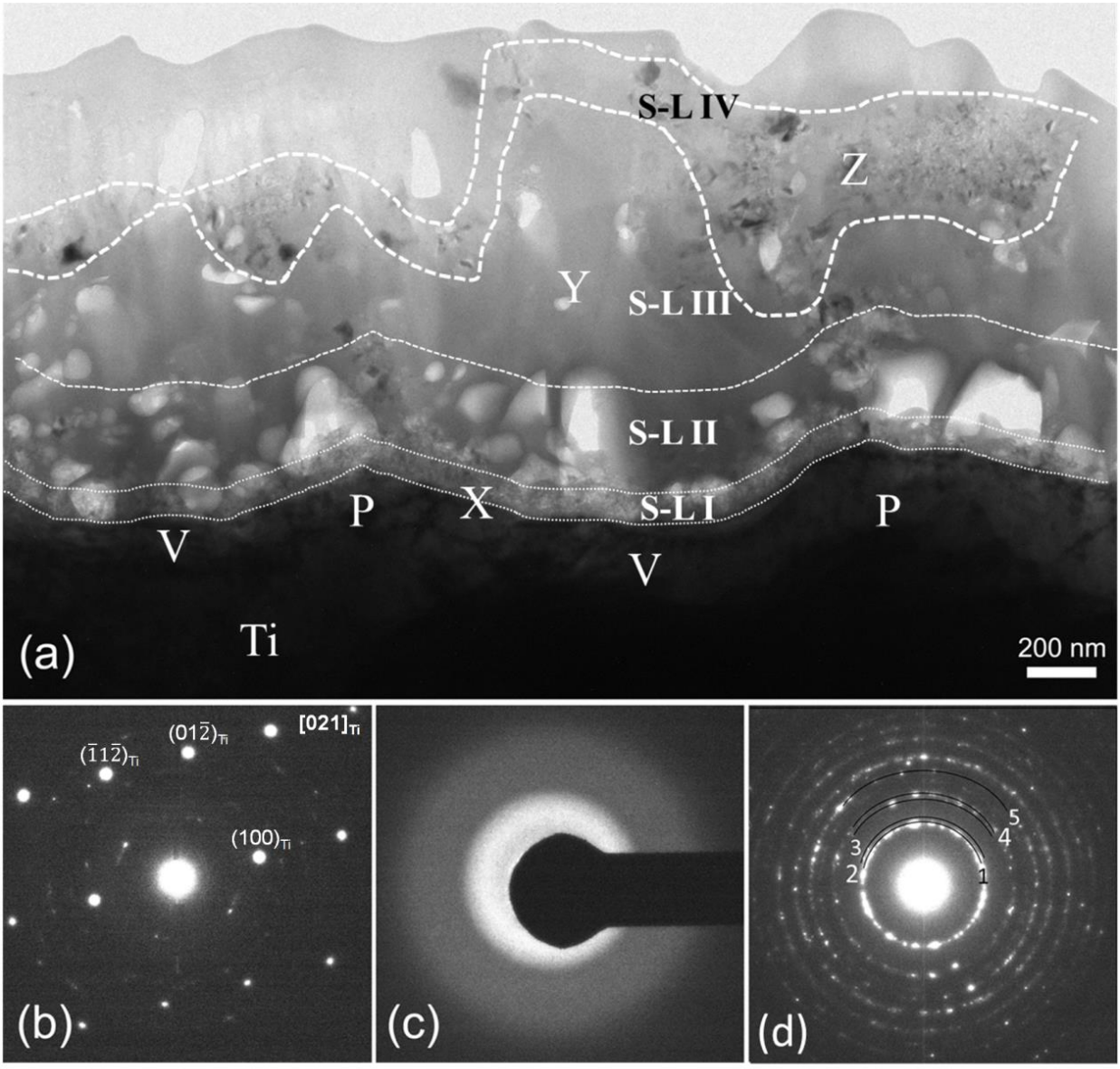

Figure 4.13 (a) A-zoom in cross-section TEM image for the coating prepared using current density 30 mA/cm^2. SAED patterns taken from (b) the interface between the coating and Ti substrate, (c) top amorphous layer and (d) crystalline layer of the coating.

Figures 4.13 (b), (c) and (d) show SAED patterns taken from the regions X, Y and Z, respectively. Figure 4.13(b) shows an overlap EDP of the [021] zone of Ti substrate and the SL I confirm the presence of the nanocrystalline structure in SL I. Figure 4.13(c) shows a pure amorphous structure in region B within the SL III, while Figure 4.13(d) presents a crystalline structure for the SL IV. The diffraction rings 1, 4, 5 in Figure 4.13(d) have a lattice spacing of 3.52 Å, 2.33 Å, 1.89 Å which can be determined to be the (101), (112), and (200) diffractions of TiO_2 anatase structure, respectively [98]. The diffraction rings 2 and 3 have a lattice spacing of 3.25 Å and 2.49 Å, corresponding to the (110) and (101) diffraction of the TiO_2 rutile structure, respectively [99]. This result indicates the coexistence of both TiO_2 rutile and anatase structure in this layer.

Figure 4.14(a) is a bright-field TEM image of the crystalline structure in the SL IV sublayer within the coating prepared using 30 mA/cm^2. The grain size in this image varies from 10 to 50 nm. The part marked by "A" has an anatase structure, while that marked by "R" has a rutile structure. It looks like that the rutile structure tends to form in larger size particles, which is consistent with ART findings [47] . It in indicated that grains nucleate as anatase can transform to rutile at high temperatures and grain growth occur during the process. Figure 4.14(b) is a HRTEM image taken from the nearby area of the particle R in Figure 4.14(a)

showing the presence of both rutile and anatase structure. The lattice fringes in grains marked by a_1, a_2, a_3, and a_4 have a lattice spacing of 3.5 Å and are identified as the (101) of the anatase structure, while the lattice fringes in grain R have a lattice spacing of 3.25 Å that can be identified as the (110) of the rutile structure. Figure 4.14(c) is a HRTEM image of the interface region between the Ti substrate and SL I showing two nanoparticles (a_5 and a_6) embedded in the amorphous matrix. The fringes of nanoparticle a_5 have a lattice spacing of ~3.5 Å corresponding the (101) of TiO_2 anatase structure while those of nanoparticle a_6 have a lattice spacing of ~2.4 Å corresponding the (103) of TiO_2 anatase structure. Nanocrystals with a rutile structure were not found in SL I nearby the interface. Formation of anatase grains around the pores can be attributed to the low activation energy of crystal formation for anatase while rutile with high activation energy develop away from pores.

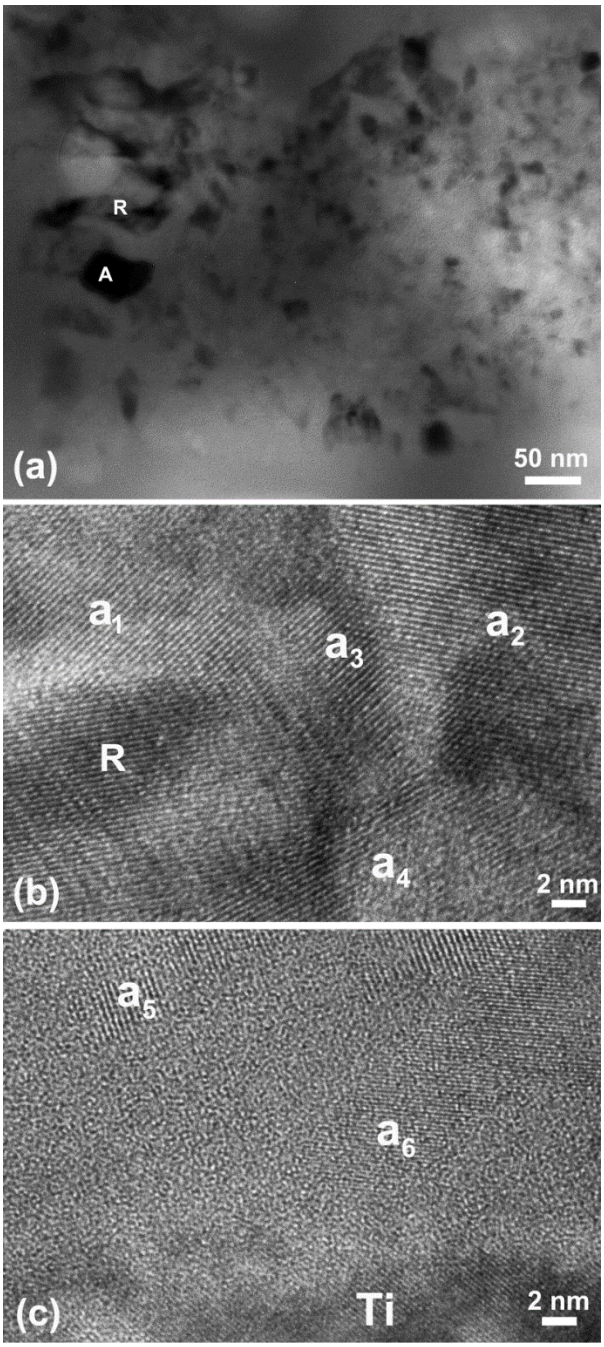

Figure 4.14 Bright-field TEM image of the crystalline structure in SL IV of the coating prepared at 30 mA/cm^2, (b) HRTEM image taken from the nearby area of R particle in (a) and (c) HRTEM image of the interface region between Ti substrate and the SL I.

The microstructure of the bottom complex layer in the coating prepared using a current density of 80 mA/cm^2 was quite similar to that prepared using 30 mA/cm^2 and can also be classified into four layers, similar to those shown in Figure 4.13(a). Figure 4.15(a) is a cross-section TEM image of a region near the interface in the coating prepared using 80 mA/cm^2 showing a dense fine nanocrystalline sublayer (SL I), a high density nanoporous sublayer (SL II) and an amorphous sublayer (SL III). The dense fine nanocrystalline sublayer (SL I) has a thickness of 290 nm and can be further classified into two layers $\boldsymbol{I_a}$ and $\boldsymbol{I_b}$**.** Figure 4.15(b) is a magnified TEM of Figure 4.15(a) showing the detail structure of the two layers $\boldsymbol{I_b}$ and $\boldsymbol{I_a}$ and its interface with the Ti substrate. The layer $\boldsymbol{I_a}$ has a thickness of ~30 nm and presents a high dense continuous structure without pores and visible boundaries. Electron diffraction analysis shows that the crystals in the coating prepared using 80 mA/cm^2 have an anatase structure, Figure 4.15(c). The layer $\boldsymbol{I_b}$ consists of nanocrystals with a size of about ~5-15 nm, between which discrete boundaries, nano or subnano cracks were formed. Figure 4.15(d) is a HRTEM taken from layer $\boldsymbol{I_a}$ presenting closely packed nanocrystalline with a size of a few nanometers.

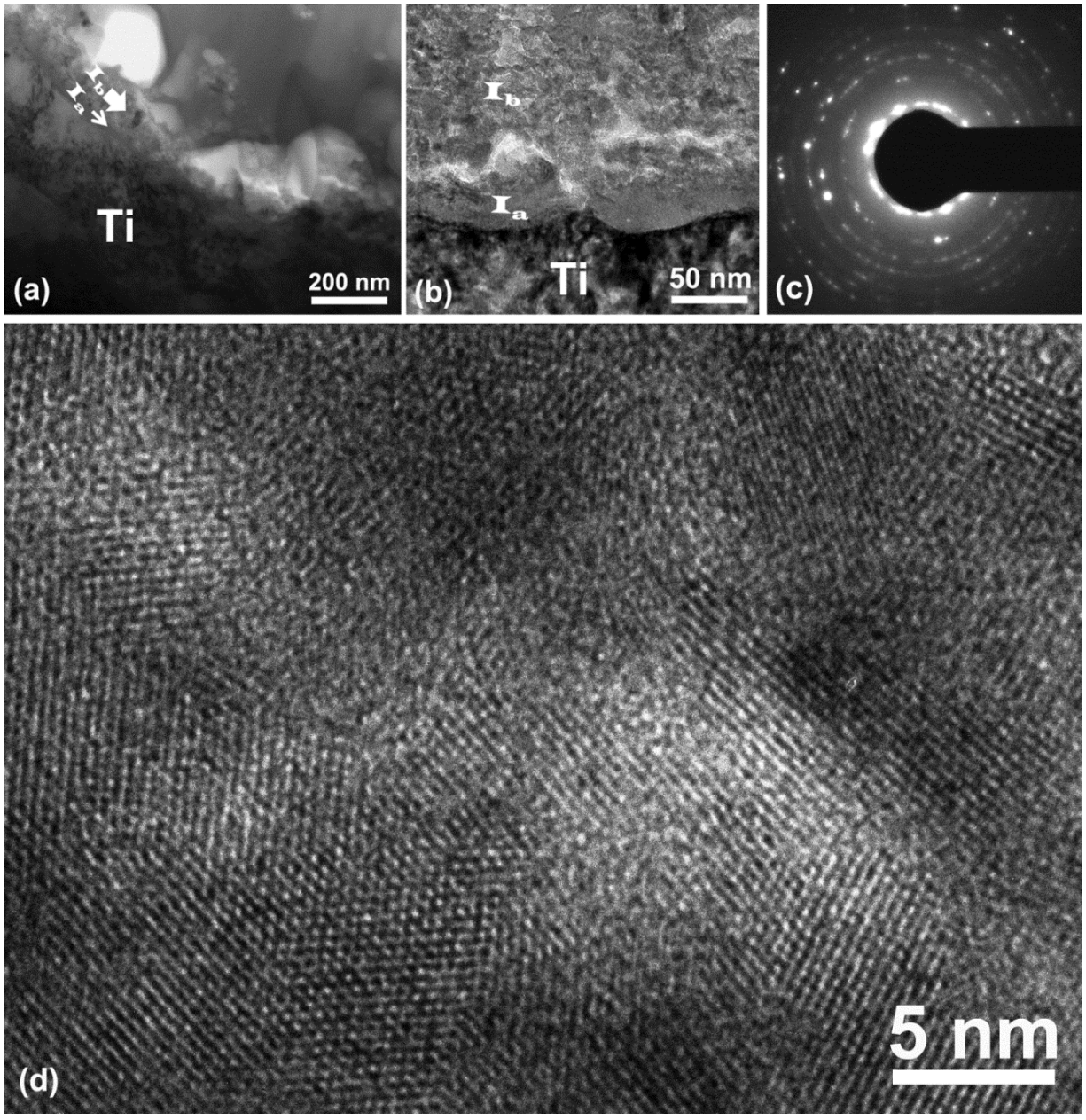

Figure 4.15 (a) Cross-section TEM image of a region near the interface of the coating prepared using 80 mA/cm^2, (b) Enlarged TEM image of the interface, (c) SAED pattern taken from the SL I and (d) HRTEM image of the layer I_a in (b).

Figure 4.16(a) is a cross-section TEM image of the bottom complex layer in the coating prepared using a current density of 120 mA/cm^2. The four distinct sublayers observed in the coatings prepared using a current density of 30 and 80 mA/cm^2 are not clearly seen in Figure 4.16(a). The four sublayers are blended. It can be found that the crystals formed in this coating have a TiO_2 anatase structure as identified by both SAED and XRD. The amount of the crystalline structure in this coating is more than that in the previous coatings and is distributed irregularly. Figure 4.16(b) is an enlarged TEM image of a region near the interface presenting fine nanocrystals close to the Ti substrate and coarse nanocrystals away from the Ti, such as grains marked by D_1 and D_2. The size of the coarse grains D_1 and D_2 is ~300 nm and 500 nm, respectively. Electron diffraction analysis shows that each coarse grain has a single crystal structure. Figure 4.16(c) is a TEM image from the coating/Ti interface showing nano-porous rich cluster structure. This nanoporous cluster is surrounded by an amorphous structure and is composed of high dense nano pores and TiO_2 anatase nanocrystals. Figure 4.16(d) shows EDS spectra from the crystalline region, amorphous located in the middle and the top of the coating. The crystalline regions are P free, while the amorphous regions consist of a certain amount of P. The amorphous region on the top of the coating consists of more P than that located in the middle section of the coating. Higher P on the top of the coating can be attributed to the low mobility of phosphorous species which cannot diffuse though the oxide and

remain on the top layer, as opposed to the oxygen ions with higher mobility which diffuse throughout the coating.

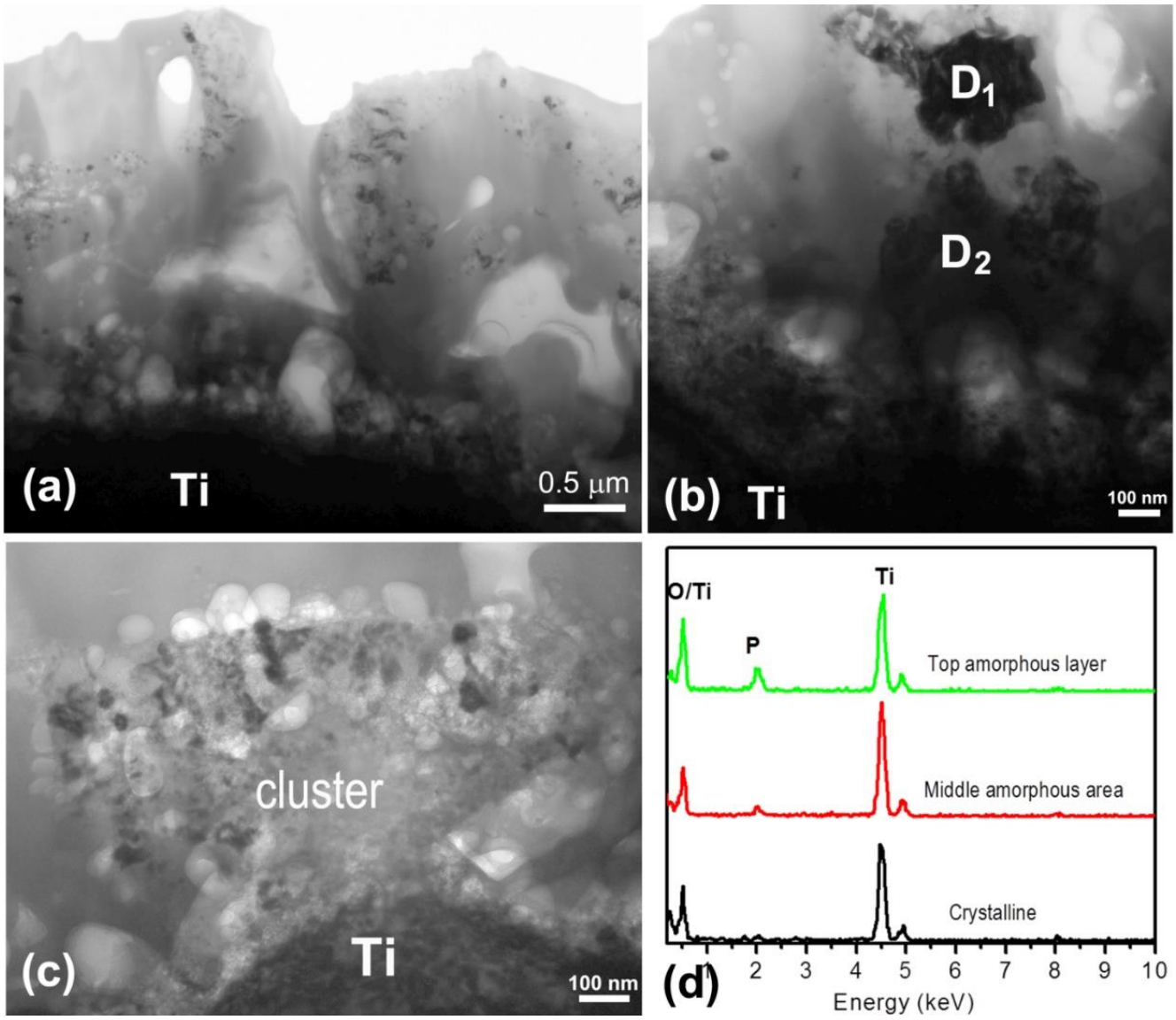

Figure 4.16(a) Cross-section TEM image of the bottom complex layer of the coating processed at 120 mA/cm^2; (b) and (c)enlarged TEM image of a region near the interface showing large nanocrystals and a nano-porous cluster, respectively; (d) EDS spectra taken from the crystalline area, amorphous regions located in the middle and top of the coating.

4.2.5 XPS Analysis

XPS studies were conducted in an effort to further investigate the nature of the top amorphous layer that was observed in all PEO treated samples. Figure 4.17 shows high resolution spectra for the sample processed at 30 mA/cm^2. Figure 4.17(a) presents the high resolution spectrum of the Ti*2p* peak. The Ti*2p* spectrum of the coating mainly consists of two peaks, which correspond to the $2p_{1/2}$ and $2p_{3/2}$ spin orbital doublet peaks in Ti-O-Ti located at 464.5 eV and 458.8 eV, respectively. The two contributions are separated by 5.7 eV, which is in agreement with spin-orbit splitting values reported previously [100]. Figure 4.17(b) shows the high-resolution spectra of the P*2p* peak. The peak at 133.5 eV is the main assignment of P in PO_4^{3-} [101]. Figure 4.17(c) shows the high resolution XPS spectra for oxygen. O1s can be deconvoluted to 3 peaks at 531.4, 532.2, and 533.3 eV. The peak at 531.4 eV corresponds to Ti-O-P and the peak at 532.2 is associated to the P-O-H. The results revealed that the atomic ratio of Ti-O-P to P-O-H is 2. Also, the peak at 533.3 eV corresponds to O-C due to the coating contamination [102].

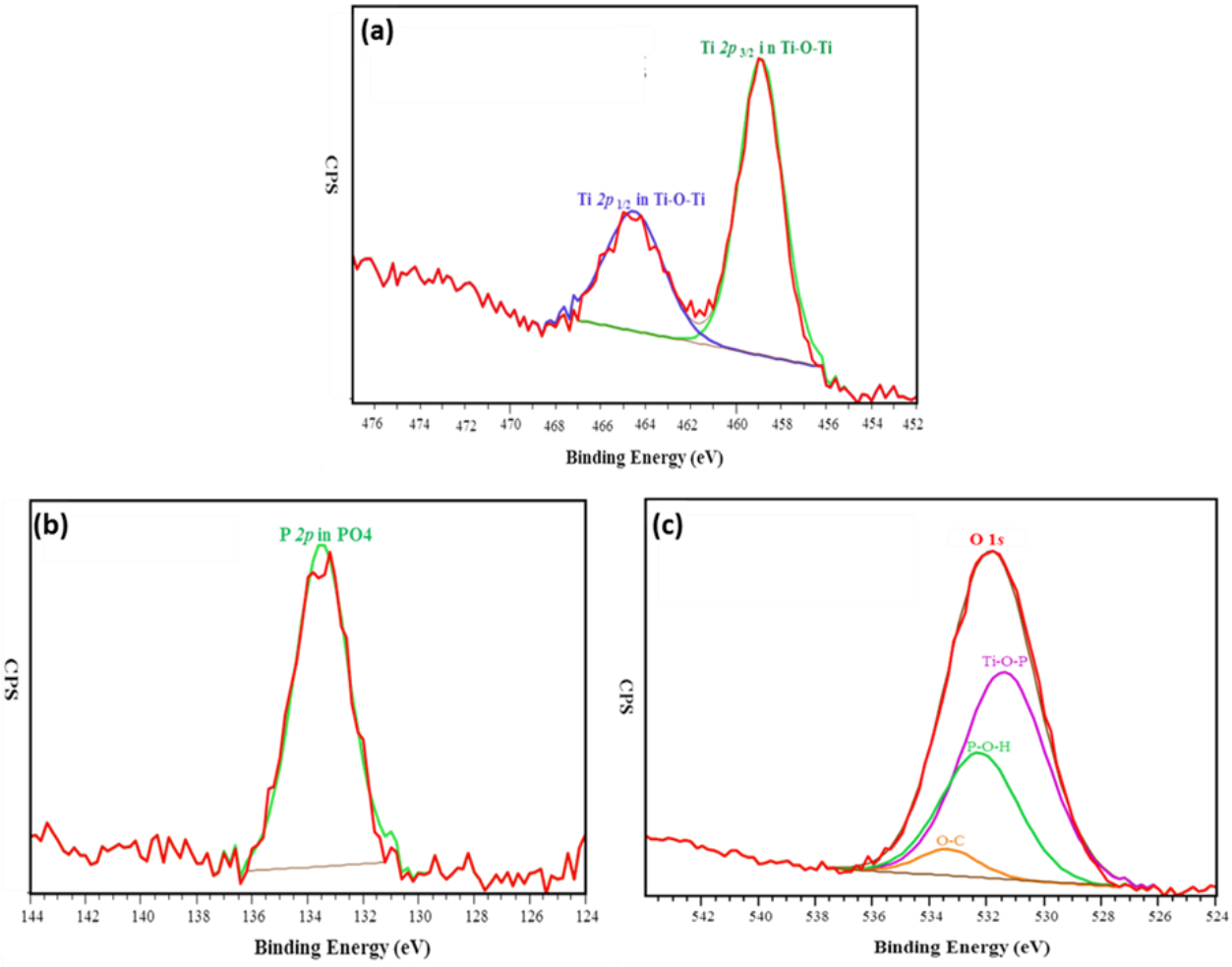

Figure 4.17 Typical high resolution XPS spectra of peak (a) Ti 2p (b) P 2p and (c) O 1s of the PEO coated samples coated at 30 mA/cm^2.

Based on the present results TiO_2 and PO_4^{3-} are present in the top layer of the coatings. Also, the oxygen high resolution spectrum illustrates that oxygen has been bonded with titanium, phosphorous and hydrogen. This would suggest the presence

of amorphous titanium hydrogen phosphate compound like Ti $(HPO_4)_2$ on the top layer of the coating [98, 103].

In this study, a range of current densities were applied in the same electrolyte and their effect on ionic/electronic current contribution rate and growth mechanism were studied. Investigations in chapter 2 showed that electrolyte composition plays a significant role on electrochemical reactions. The knowledge gained in this chapter can be employed to further investigate electrolyte composition effect on coating growth mechanism, which will be presented in the next chapter.

Chapter 5

Effect of Electrolyte Chemistry on Ionic/Electronic Current

As it is shown in literature review, many studies have been conducted on the effect of electrolyte chemistry on coating properties. However, the reason why coatings produced in different electrolytes exhibit different properties along with the underlying mechanism have not been fully understood. Here, the acquired knowledge from the previous part of the study is used to develop a better understanding of the role of electrolyte chemistry on ionic and electronic current and coating growth mechanism. Thus, an electrolyte was selected with higher conductivity in an effort to explore its effect on ionic and electronic currents.

5.1 Experiment

Coatings were prepared in a stable alkaline electrolyte containing $K_4P_2O_7$ (1.7 g/l), Na_2CO_3 (1.7 g/l), and KOH (1.2 g/l) with conductivity of 8.7 mS/cm and pH of 12. The coatings prepared in this electrolyte are denoted as C. These PEO coatings were compared to those that have been studied in the previous section. The latter electrolyte was consisting of $K_4P_2O_7$ (3.4 g/l) and KOH (1.2 g/l) at pH= 12 with a conductivity of

7.1 mS/cm. The produced coatings in this electrolyte are denoted as P. Treatments are conducted at 30 mA/cm^2 and 120 mA/cm^2 for both electrolytes.

5.2 Voltage- Time Response

V-t response of the C and P coatings processed at 30 mA/cm^2 and 120 mA/cm^2 is presented in Figures 5.1(a) and (b), respectively. Figure 5.1(a) shows at 30 mA/cm^2 long processing times can be obtained and all three stages of the coating formation are visible for both C and P coatings. Furthermore, at this current density, the electronic current is dominant. As can be seen, by increasing the current density, processing time decreased and only the first stage of the coating growth was evident for both coatings. It is shown that the breakdown voltage of the PEO coatings developed in P and C electrolytes is 269 V and 302 V, respectively. The proposed model for breakdown explains that during the PEO process, the electrolyte species enter the oxide as charged particles. These anions, once incorporated into the oxide, behave as impurity centers. Due to the high electric field, ***E,*** these centers can be ionized, releasing a current of electrons into the oxide conduction band. According to the earlier breakdown theories, these electrons, once in the conduction band, are accelerated by the anodization field producing avalanches and plasma. Therefore, electrolyte characteristics including conductivity and composition can affect the voltage where sparks start to occur

(breakdown voltage). According to the Ikonopisov model, breakdown voltage is represented by the following equation [104]:

$$V_b = a_B + b_B \log\left(\frac{1}{k}\right) \quad (5.1)$$

Where k is the electrolyte conductivity and a_B and b_B are constants for a given metal and electrolyte composition. It can be concluded that difference in breakdown voltage in P and C can be attributed to the difference in electrolyte conductivities and compositions. Anions like PO_4^{3-} in P and CO_3^{2-} in addition to the phosphate ions in C are incorporated into the oxide. It is suggested that by increasing the electrolyte conductivity, larger number of ions react and diffuse through the oxide which increases the ionic current incorporation rate. As it was discussed earlier, all the PEO stages are not present at high current densities and it is hard to find the breakdown voltage in Figure 5.1(b).

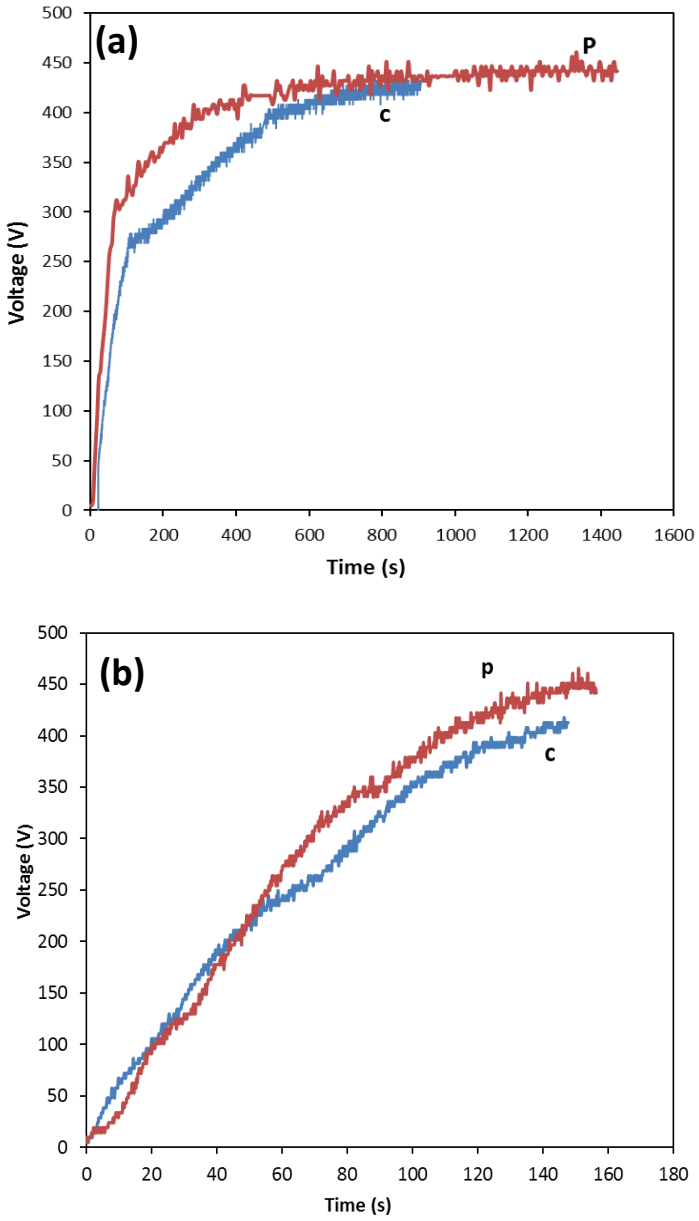

Figure 5.1 Voltage vs. time plots of C and P samples processed at current densities of (a) 30 and (b)120 mA/cm^2.

5.3 Characterization

SEM micrographs of the coatings produced in different electrolytes at 30 mA/cm^2 are presented in Figure 5.2(a) and at 120 mA/cm^2 in Figure 5.2(b). As it is shown, at constant current, coatings prepared in P, develop a greater number of pores than in C. Porosity percentage of the coatings is presented in Table 5.1. This phenomenon can also be ascribed to the higher incorporation rate of ionic charge in C in which large number of ions diffuse through discharge channels, fill these channels and form denser oxides. Also, it is suggested that as breakdown voltage increases, energy of plasma discharges increase which results in formation of larger discharge channels and pores [14] . At 120 mA/cm^2, due to the fact that incorporation of the ionic charge is already high at elevated currents, increasing the ionic charge does not have much influence on porosity percentage, and more intense arcs was observed in shorter time in C.

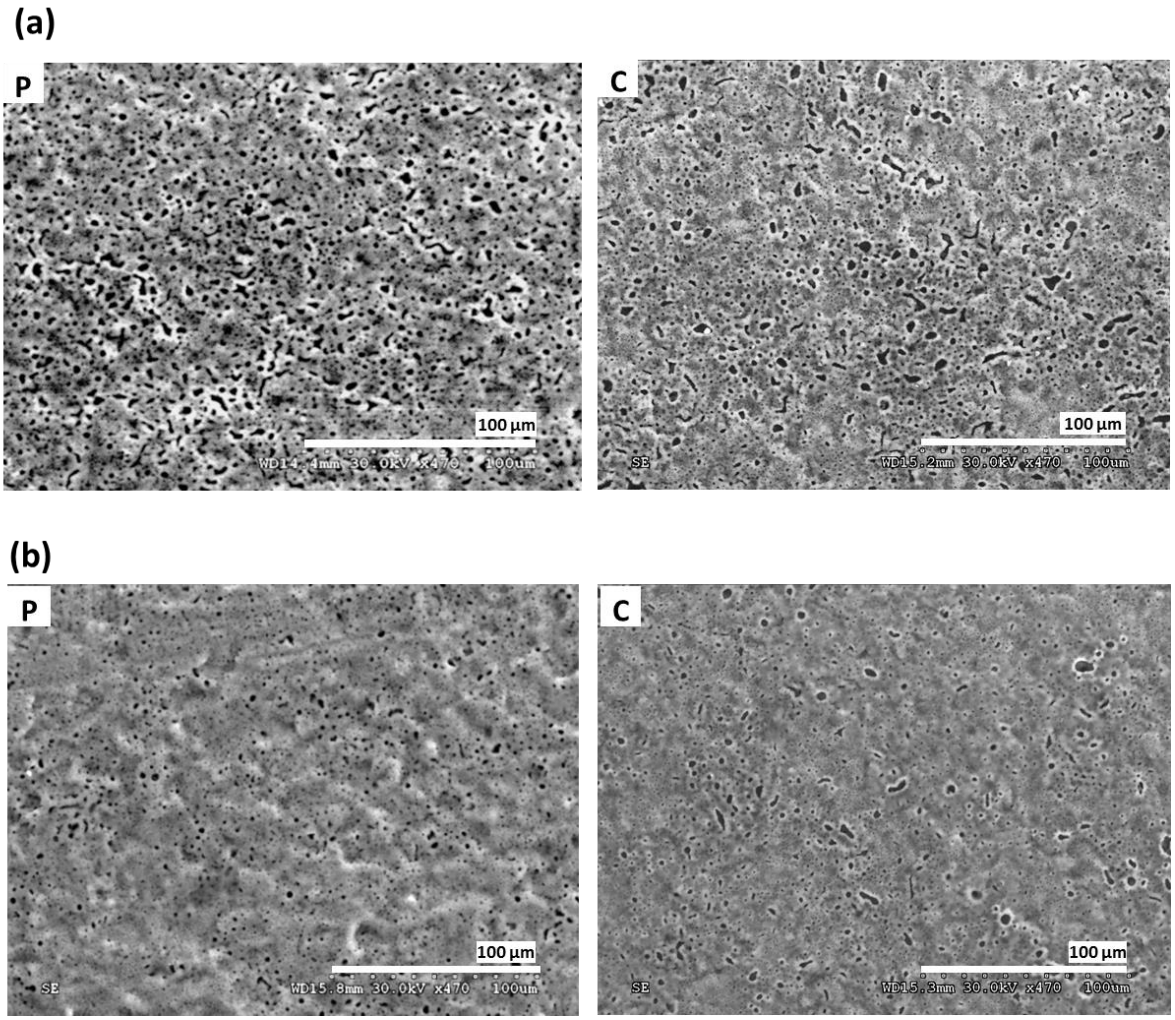

Figure 5. 2 Surface morphologies of PEO coated samples of C and P at current densities of (a) 30 and (b) 120 mA/cm^2.

Figure 5.3 presents cross sectional SEM images of the PEO coatings deposited in C at selected current densities. The average coating thickness is 6.6 and 6.8 μm respectively for the coatings processed at 30 mA/cm^2 and 120 mA/cm^2. Coating characteristics are presented in Table 5.1. It is shown that thickness and growth rate of the coatings processed in C, at constant current, are higher than in P. This phenomenon can be attributed to the higher contribution of ionic charge in C. The ratio of the effective ionic charge to the total charge is calculated as it is described before and presented in Table 5.1.

Table 5.1 Conductivity, growth rate, effective ionic charge incorporation rate, porosity, mean roughness and surface index of coated samples in C and P electrolytes at different current densities.

Current density (mA/cm^2)	Electrolyte	Conductivity (mS/cm)	Growth rate (nm/s)	$\frac{Q\text{effective ionic}}{Q\text{total}}$	Porosity %	R_a (μm)	Surface index
30	P	7.1	1.54	0.11	20.1	2.1	7.12
30	C	8.7	7.11	0.48	12.8	1.8	3.96
120	P	7.1	33.19	0.51	7.9	1.5	5.53
120	C	8.7	41.41	0.71	9.4	1.6	3.38

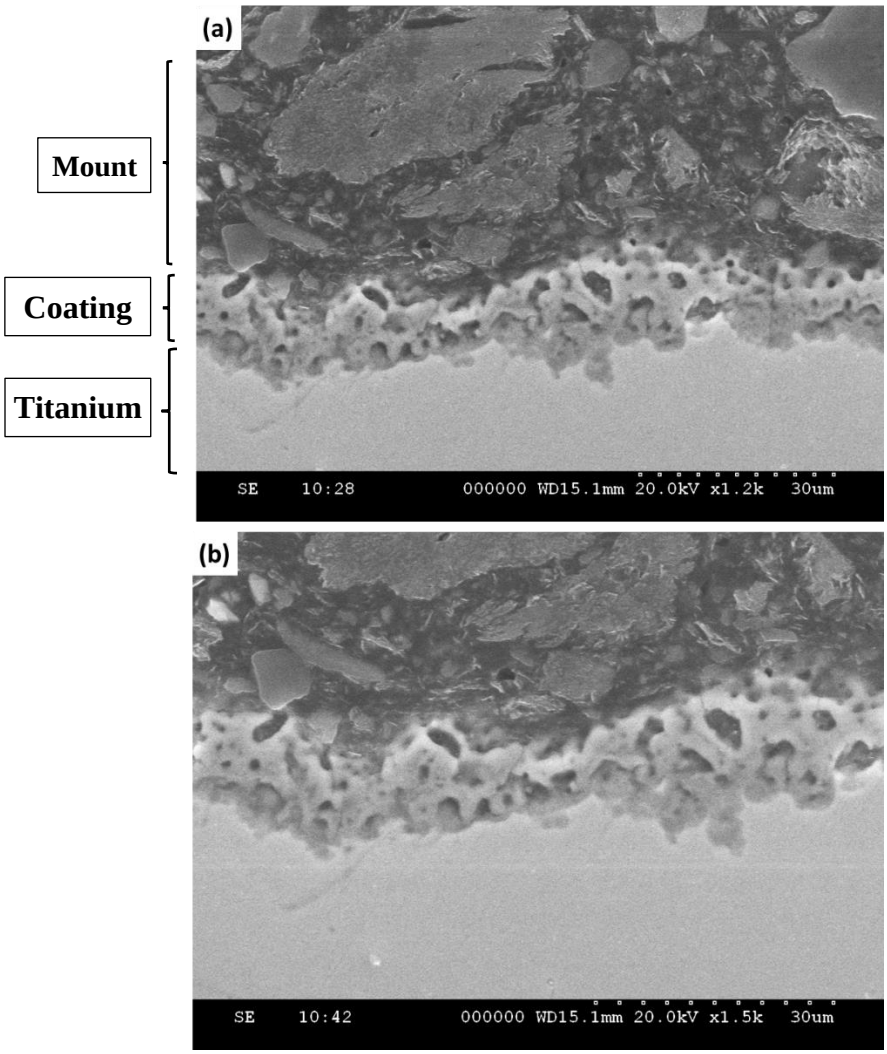

Figure 5.3 SEM cross-section images of C coatings at current densities of (a) 30 and (b) 120 mA/cm^2.

Figure 5.4 illustrates the surface topography of the produced layers on CP Ti processed in electrolyte C at the selected current densities. Coating surfaces for both current densities look similar and smooth. In order to obtain a better understanding of

the topography, the average roughness (R_a) and surface index (ratio of actual surface area/nominal area) of the coatings processed in C and P electrolytes are presented in Table 5.1. The results showed that the mean roughness and surface index, at constant current density, is higher in coatings prepared in electrolyte P than those in C explain the result of higher contribution of electronic charge in P and generation of higher amounts of pores.

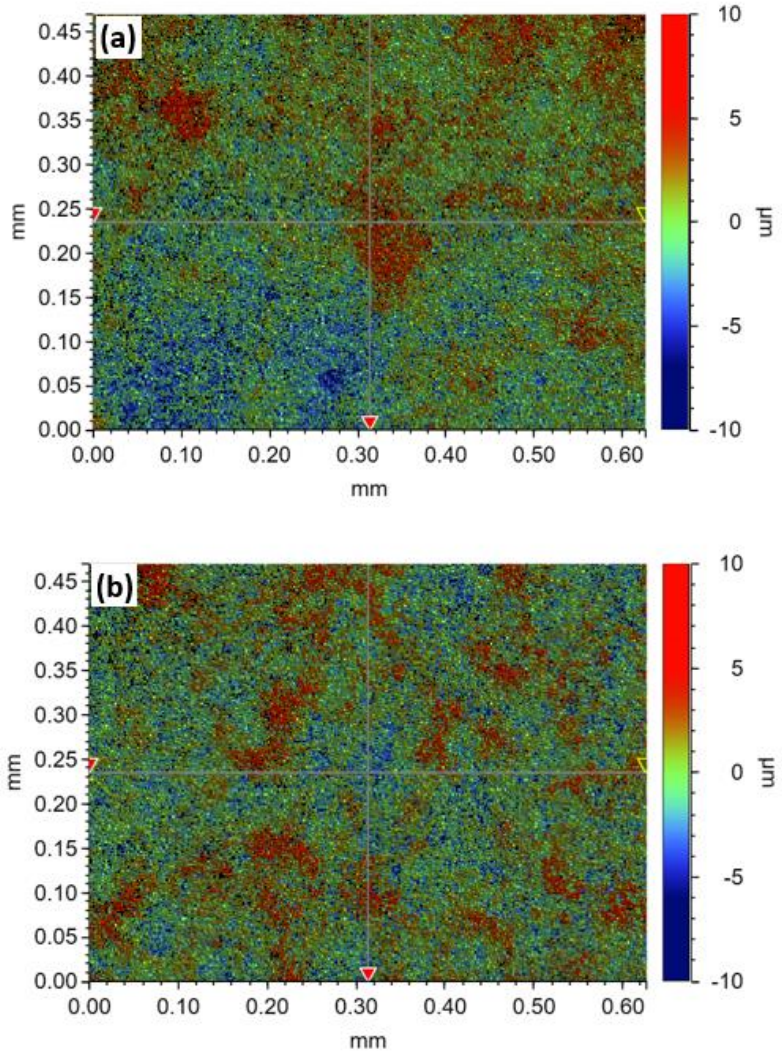

Figure 5.4 Surface profile using white light interferometry of the PEO-coated samples in C electrolyte at current densities of (a) 30 (b) 120 mA/cm^2.

XRD patterns of the P and C coatings prepared at 30 mA/cm^2 are presented in Figure 5.5(a) and (b), respectively. The peaks (marked by "Δ") at 2θ angles of 25.25°, 48.06°, and 62.68° have a lattice spacing of 3.52 Å, 1.89 Å, and 1.48 Å and can be ascribed, respectively, to the (101) and (200) and (204) planes of anatase TiO_2 structure. The peaks (marked by "O") at 2θ angles of 27.8° and 54.36° having a lattice spacing of 3.25 Å and 1.68 Å corresponds to the (110) and (211) planes of rutile TiO_2, respectively. The peaks (marked by "*") are diffraction peaks of the Ti substrate. XRD results indicate that anatase TiO_2 structure was formed in all coatings, while rutile TiO_2 structure was only formed in the coating produced in P electrolyte using 30 mA/cm^2. Formation of rutile phase in phosphate electrolyte can be caused by formation of large number of plasma discharges and high contribution of electronic charge at this condition which provide enough temperature for rutile formation.

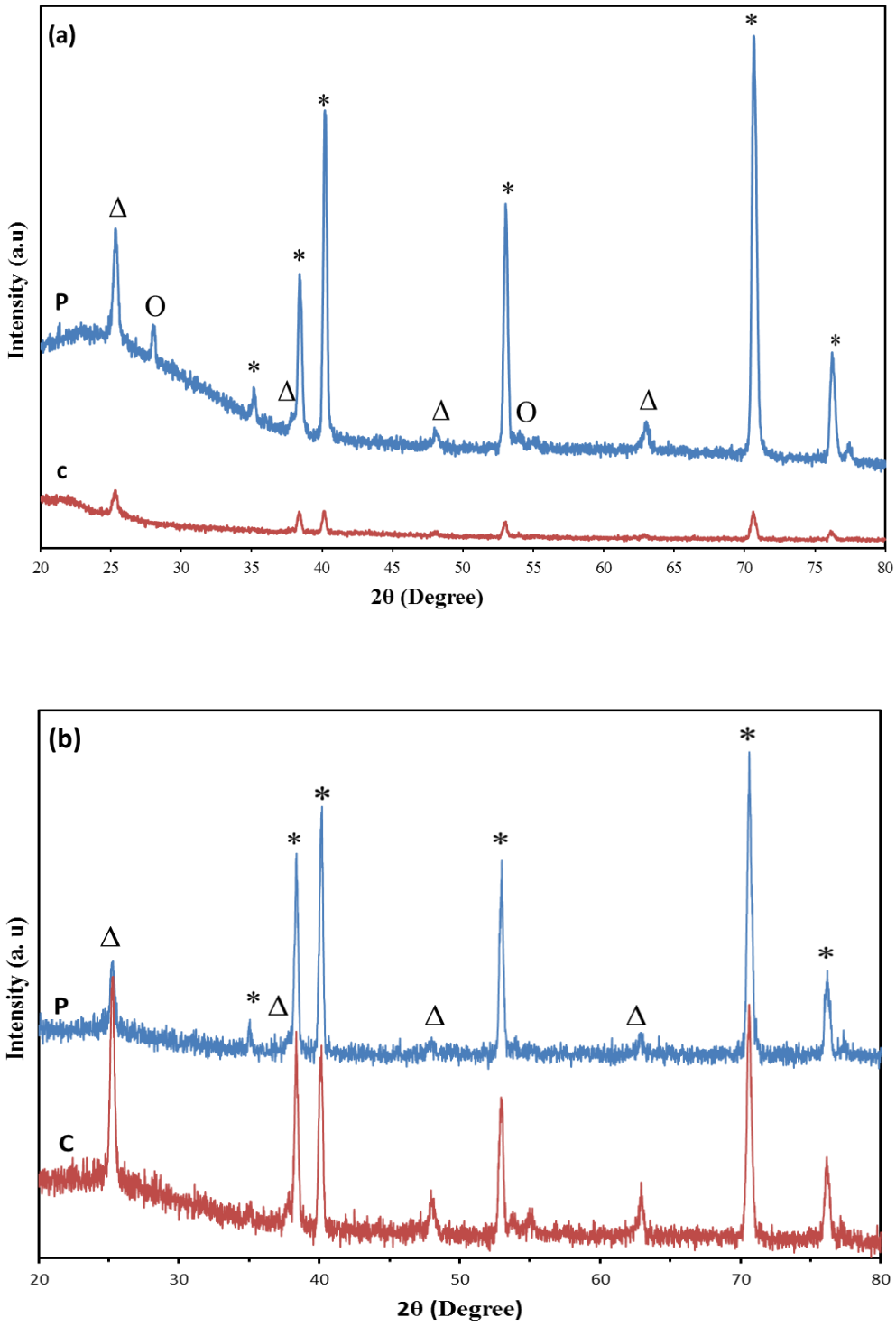

Figure 5.5 XRD patterns of the coatings formed in P and C electrolytes at current densities of (a) 30 and (b) 120 mA/cm^2.

It is shown that electrolyte properties including composition and conductivity have significant effects on breakdown voltage and contribution of the ionic charge and as a result coating characteristics. It is found that changing electrolyte composition with higher levels of conductivity can have similar effect as increasing current density in terms of elevating ionic charge incorporation rate and formation of dense oxides with high growth rate.

Chapter 6

Summary of PEO Mechanism

Understanding the PEO mechanism is essential to produce coatings with desirable characteristics for a variety of new applications. Total applied current to the oxide, in this process, is composed of electronic current caused by sparking and ionic current caused by diffusion of electrolyte ions into the oxide. It was found that at low current densities (30 and 40 mA/cm^2), the contribution of ionic current is very small. This means that a large number of discharge channels, develop in the oxide, but there are not enough ions to diffuse through them and react which leads to the formation of limited thickness titanium oxide. High density of plasma discharges at this condition, form large number of discharge channels and increase the porosity and surface roughness of the coating. Also, these discharges provide enough energy to raise temperature facilitating formation of both rutile and anatase. For the coatings processed at intermediate values (50 to 100 mA/cm^2), the incorporation rate of ionic current increases, but there is a moderate number of ions for oxide formation and the contribution of electronic current is still higher. Moving to the higher current densities (120 and 140 mA/cm^2), balanced (almost equal) amounts of ionic and electronic

current prevailed. This case resulted in the highest growth rate presenting an optimum balance of ionic and electronic currents. It was concluded that in order to achieve high growth rates, equal or balanced contributions from ionic (diffusion of ions to the channels for reaction) and electronic (generation of fine channels) charges are required. At this condition, oxide developed much faster and a more uniform and dense anatase coatings were formed. Moreover, TEM studies showed all coatings are composed of two layers: an amorphous layer on the top and a composite layer close to the substrate. The bottom composite layer has a complex microstructure consisting of nanocrystalline structure, amorphous structure and nano pores. An amorphous phase forms at the coating/electrolyte interface, and its thickness is constant (~700-800 nm) regardless of the coating condition. It is suggested that presence of P, constant cooling of the electrolyte and low thermal conductivity of the oxide may inhibit the top layer of the coating from forming a crystalline phase. When an envelope of an oxygen bubble forms on the anodic surface other anions like phosphate, accumulate on these bubbles close to the anode due to the high electric field. After plasma bubble formation, these bubbles implode and oxygen ions are thrown to the surface, react and form the oxide. This process followed by transfer of phosphate ions with lower mobility which remain on the surface, freeze and form amorphous phase. The thickness ratio between the bottom complex layer and the top amorphous layer increases by increasing the applied current density. The percentage of crystalline area for the samples processed at 30, 80, and 120 mA/cm^2 is about 18%, 56%, and 64%,

respectively. Furthermore, the effect of electrolyte composition on ionic and electronic current and coating growth mechanism was investigated. It is shown that electrolyte properties including composition and conductivity have significant effects on breakdown voltage and contribution of the ionic charge and as a result coating characteristics. It is found that changing electrolyte composition with higher levels of conductivity can have similar effect as increasing current density in terms of elevating ionic current incorporation rate and formation of dense oxides with high growth rate.

Chapter 7

Conclusion

- The present research revealed clearly that both the electronic and ionic currents play crucial roles in the PEO process and a balanced contribution of them is needed to realize the benefits in the oxide growth process.
- It was found that at low current densities, the contribution of electronic current is dominating. Large number of discharge channels at this condition increases the porosity and surface roughness of the coating. Also, these discharges provide enough energy to raise the temperature facilitating formation of both stable rutile and metastable anatase phases.
- By increasing the current density, the incorporation rate of ionic current increases which results in the formation of dense anatase coatings with high growth rates.
- TEM studies showed that all coatings are composed of two layers: an amorphous layer on the top and a composite layer close to the substrate. An amorphous phase forms at the coating/electrolyte interface, and its thickness is constant (~700-800 nm) regardless of the processing conditions.
- It was shown that electrolyte properties including composition and conductivity have significant effects on breakdown voltage and contribution of the ionic charge and as a result coating characteristics.

- The results showed a clear correlation between the role of ionic current and electronic current, obtained from v-t response, and coating growth mechanism and characteristics.

References

[1] P. Huang, K.-W. Xu, Y. Han, Preparation and apatite layer formation of plasma electrolytic oxidation film on titanium for biomedical application, Materials Letters 59(2–3) (2005) 185-189.

[2] A. Yerokhin, X. Nie, A. Leyland, A. Matthews, Characterisation of oxide films produced by plasma electrolytic oxidation of a Ti–6Al–4V alloy, Surface and Coatings Technology 130(2) (2000) 195-206.

[3] M. Aliofkhazraei, A.S. Rouhaghdam, T. Shahrabi, Abrasive wear behaviour of Si_3N_4/TiO_2 nanocomposite coatings fabricated by plasma electrolytic oxidation, Surface and Coatings Technology 205 (2010) 41-46.

[4] S. Tsunekawa, Y. Aoki, H. Habazaki, Two-step plasma electrolytic oxidation of Ti–15V–3Al–3Cr–3Sn for wear-resistant and adhesive coating, Surface and coatings Technology 205(19) (2011) 4732-4740.

[5] B. Pabón, J. Beltrán, G. Sánchez-Santolino, I. Palacio, J. López-Sánchez, J. Rubio-Zuazo, J. Rojo, P. Ferrer, A. Mascaraque, M. Muñoz, Formation of titanium monoxide (001) single-crystalline thin film induced by ion bombardment of titanium dioxide (110), Nature communications 6 (2015) 6147.

[6] M. Hosseini, S. Sajjadi, M. Momeni, Electrodeposition of platinum metal on titanium and anodised titanium from P salt: application to electro-oxidation of glycerol, Surface Engineering 23 (2013) 419-424.

[7] A. Matthews, Titanium nitride PVD coating technology, Surface Engineering 1 (2013) 93-104.

[8] M. Goudarzi, F. Batmanghelich, A. Afshar, A. Dolati, G. Mortazavi, Development of electrophoretically deposited hydroxyapatite coatings on anodized nanotubular TiO2 structures: Corrosion and sintering temperature, Applied Surface Science 301 (2014) 250-257.

[9] F. Batmanghelich, M. Ghorbani, Effect of pH and carbon nanotube content on the corrosion behavior of electrophoretically deposited chitosan–hydroxyapatite–carbon nanotube composite coatings, Ceramics International 39(5) (2013) 5393-5402.

[10] J.M. Wheeler, J.A. Curran, S. Shrestha, Microstructure and multi-scale mechanical behavior of hard anodized and plasma electrolytic oxidation (PEO) coatings on aluminum alloy 5052, Surface and Coatings Technology 207 (2012) 480-488.

[11] A. Smith, R. Kelton, E.I. Meletis, Deposition of Ni Coatings by Electrolytic Plasma Processing, Plasma Chemistry and Plasma Processing 35(6) (2015) 963-978.

[12] P. Gupta, G. Tenhundfeld, E.O. Daigle, D. Ryabkov, Electrolytic plasma technology: Science and engineering—An overview, Surface and Coatings Technology 201(21) (2007) 8746-8760.

[13] A.L. Yerokhin, X. Nie, A. Leyland, A. Matthews, S.J. Dowey, Plasma electrolysis for surface engineering, Surface and Coatings Technology 122(2–3) (1999) 73-93.

[14] M. Shokouhfar, C. Dehghanian, M. Montazeri, A. Baradaran, Preparation of ceramic coating on Ti substrate by plasma electrolytic oxidation in different electrolytes and evaluation of its corrosion resistance: Part II, Applied Surface Science 258(7) (2012) 2416-2423.

[15] K. Venkateswarlu, N. Rameshbabu, D. Sreekanth, M. Sandhyarani, A. Bose, V. Muthupandi, S. Subramanian, Role of electrolyte chemistry on electronic and in vitro electrochemical properties of micro-arc oxidized titania films on CpTi, Electrochimica Acta 105 (2013) 468-480.

[16] H. Jiang, Z. Shao, B. Jing, Effect of electrolyte composition on photocatalytic activity and corrosion resistance of micro-arc oxidation coating on pure titanium, Procedia Earth and Planetary Science 2 (2011) 156-161.

[17] Y. Gao, A. Yerokhin, E. Parfenov, A. Matthews, Application of Voltage Pulse Transient Analysis during Plasma Electrolytic Oxidation for Assessment of Characteristics and Corrosion Behaviour of Ca- and P-containing Coatings on Magnesium, Electrochimica Acta 149 (2014) 218-230.

[18] A.L. Yerokhin, A. Shatrov, V. Samsonov, P. Shashkov, A. Pilkington, A. Leyland, A. Matthews, Oxide ceramic coatings on aluminium alloys produced by a pulsed bipolar plasma electrolytic oxidation process, Surface and Coatings Technology 199(2–3) (2005) 150-157.

[19] P. Bala Srinivasan, J. Liang, R.G. Balajeee, C. Blawert, M. Störmer, W. Dietzel, Effect of pulse frequency on the microstructure, phase composition and corrosion

performance of a phosphate-based plasma electrolytic oxidation coated AM50 magnesium alloy, Applied Surface Science 256(12) (2010) 3928-3935.

[20] H. Duan, C. Yan, F. Wang, Effect of electrolyte additives on performance of plasma electrolytic oxidation films formed on magnesium alloy AZ91D, Electrochimica Acta 52(11) (2007) 3785-3793.

[21] F. Liu, D. Shan, Y. Song, E.-H. Han, Effect of additives on the properties of plasma electrolytic oxidation coatings formed on AM50 magnesium alloy in electrolytes containing K_2ZrF_6, Surface and Coatings Technology 206(2–3) (2011) 455-463.

[22] J.A. Curran, H. Kalkancı, Y. Magurova, T.W. Clyne, Mullite-rich plasma electrolytic oxide coatings for thermal barrier applications, Surface and Coatings Technology 201(21) (2007) 8683-8687.

[23] M. Shokouhfar, C. Dehghanian, A. Baradaran, Preparation of ceramic coating on Ti substrate by Plasma electrolytic oxidation in different electrolytes and evaluation of its corrosion resistance, Applied Surface Science 257(7) (2011) 2617-2624.

[24] O.P. Terleeva, Y.P. Sharkeev, A.I. Slonova, I.V. Mironov, E.V. Legostaeva, I.A. Khlusov, E. Matykina, P. Skeldon, G.E. Thompson, Effect of microplasma modes and electrolyte composition on micro-arc oxidation coatings on titanium for medical applications, Surface and Coatings Technology 205(6) (2010) 1723-1729.

[25] M. Montazeri, C. Dehghanian, M. Shokouhfar, A. Baradaran, Investigation of the voltage and time effects on the formation of hydroxyapatite-containing titania

prepared by plasma electrolytic oxidation on Ti–6Al–4V alloy and its corrosion behavior, Applied Surface Science 257(16) (2011) 7268-7275.

[26] K.R. Shin, Y.G. Ko, D.H. Shin, Effect of electrolyte on surface properties of pure titanium coated by plasma electrolytic oxidation, Journal of Alloys and Compounds 509, Supplement 1 (2011) 478-481.

[27] R.H.U. Khan, A.L. Yerokhin, A. Matthews, Structural characteristics and residual stresses in oxide films produced on Ti by pulsed unipolar plasma electrolytic oxidation, Philosophical Magazine 88(6) (2008) 795-807.

[28] V. Dehnavi, B.L. Luan, D.W. Shoesmith, X.Y. Liu, S. Rohani, Effect of duty cycle and applied current frequency on plasma electrolytic oxidation (PEO) coating growth behavior, Surface and Coatings Technology 226 (2013) 100-107.

[29] V. Dehnavi, X.Y. Liu, B.L. Luan, D.W. Shoesmith, S. Rohani, Phase transformation in plasma electrolytic oxidation coatings on 6061 aluminum alloy, Surface and Coatings Technology 251 (2014) 106-114.

[30] R. Arrabal, E. Matykina, T. Hashimoto, P. Skeldon, G.E. Thompson, Characterization of AC PEO coatings on magnesium alloys, Surface and Coatings Technology 203(16) (2009) 2207-2220.

[31] W. Zhang, Z. Zhu, C.Y. Cheng, A literature review of titanium metallurgical processes, Hydrometallurgy 108(3) (2011) 177-188.

[32] R. Schutz, J. Grauman, Corrosion behavior of titanium and other alloys in laboratory FGD scrubber environments, Mater. Performance;(United States) 25(4) (1986).

[33] J.H.C.L. C.N. Elias, R. Valiev, and M.A. Meyers, Biomedical applications of titanium and its alloys, JOM 60 (2008) 46-49.

[34] J. Goldberg, C.J. Burstone, An evaluation of beta titanium alloys for use in orthodontic appliances, Journal of dental research 58(2) (1979) 593-599.

[35] G. Welsch, R. Boyer, E. Collings, Materials properties handbook: titanium alloys, ASM international (1993).

[36] X. Liu, P.K. Chu, C. Ding, Surface modification of titanium, titanium alloys, and related materials for biomedical applications, Materials Science and Engineering: R: Reports 47(3) (2004) 49-121.

[37] A. Seeber, A.N. Klein, C.V. Speller, P. Egert, F.A. Weber, A. Lago, Sintering unalloyed titanium in DC electrical abnormal glow discharge, Materials Research 13 (2010) 99-106.

[38] V.A. Joshi, Titanium alloys: an atlas of structures and fracture features, Crc Press (2006).

[39] J.L. Murray, H.A. Wriedt, The O−Ti (Oxygen-Titanium) system, Journal of Phase Equilibria 8(2) (1987) 148-165.

[40] X.Z. Ding, X.H. Liu, Y.Z. He, Grain size dependence of anatase-to-rutile structural transformation in gel-derived nanocrystalline titania powders, Journal of Materials Science Letters 15(20) (1996) 1789-1791.

[41] J.A. Gamboa, D.M. Pasquevich, Effect of Chlorine Atmosphere on the Anatase-Rutile Transformation, Journal of the American Ceramic Society 75(11) (1992) 2934-2938.

[42] A. Beltran, L. Gracia, J. Andres, Density functional theory study of the brookite surfaces and phase transitions between natural titania polymorphs, The Journal of Physical Chemistry B 110(46) (2006) 23417-23423.

[43] Y.R. Park, K.J. Kim, Structural and optical properties of rutile and anatase TiO_2 thin films: effects of Co doping, Thin Solid Films 484(1) (2005) 34-38.

[44] T. Arlt, M. Bermejo, M. Blanco, L. Gerward, J. Jiang, J.S. Olsen, J. Recio, High-pressure polymorphs of anatase TiO_2, Physical Review B 61(21) (2000) 14414.

[45] J. Muscat, V. Swamy, N.M. Harrison, First-principles calculations of the phase stability of TiO_2, Physical Review B 65(22) (2002) 224112.

[46] M. Arroyo-de Dompablo, A. Morales-García, M. Taravillo, DFT+ U calculations of crystal lattice, electronic structure, and phase stability under pressure of TiO_2 polymorphs, The Journal of chemical physics 135(5) (2011) 054503.

[47] D.A. Hanaor, C.C. Sorrell, Review of the anatase to rutile phase transformation, Journal of Materials science 46(4) (2011) 855-874.

[48] R. Otsuka, Studies on the corrosion of titanium, Sc. Papers Inst. Phys. Chem. Res. (Japan), 54 (1960) 97.

[49] H. Zhang, J.F. Banfield, Understanding polymorphic phase transformation behavior during growth of nanocrystalline aggregates: insights from TiO_2, The Journal of Physical Chemistry B 104(15) (2000) 3481-3487.

[50] J. Banfield, Thermodynamic analysis of phase stability of nanocrystalline titania, Journal of Materials Chemistry 8(9) (1998) 2073-2076.

[51] G. Li, L. Li, J. Boerio-Goates, B.F. Woodfield, Grain-growth kinetics of rutile TiO_2 nanocrystals under hydrothermal conditions, Journal of materials research 18(11) (2003) 2664-2669.

[52] S.D. Sharma, D. Singh, K. Saini, C. Kant, V. Sharma, S. Jain, C. Sharma, Sol–gel-derived super-hydrophilic nickel doped TiO_2 film as active photo-catalyst, Applied Catalysis A: General 314(1) (2006) 40-46.

[53] S. Meyer, R. Gorges, G. Kreisel, Preparation and characterisation of titanium dioxide films for catalytic applications generated by anodic spark deposition, Thin Solid Films 450(2) (2004) 276-281.

[54] G. Jellison Jr, L. Boatner, J. Budai, B.-S. Jeong, D. Norton, Spectroscopic ellipsometry of thin film and bulk anatase (TiO_2), Journal of Applied Physics 93(12) (2003) 9537-9541.

[55] K. Tanaka, M.F. Capule, T. Hisanaga, Effect of crystallinity of TiO_2 on its photocatalytic action, Chemical Physics Letters 187(1-2) (1991) 73-76.

[56] M. Grätzel, The artificial leaf, molecular photovoltaics achieve efficient generation of electricity from sunlight, Comments on Inorganic Chemistry 12(2-3) (1991) 93-111.

[57] S.D. Mo, W. Ching, Electronic and optical properties of three phases of titanium dioxide: Rutile, anatase, and brookite, Physical Review B 51(19) (1995) 13023.

[58] O. Carp, C.L. Huisman, A. Reller, Photoinduced reactivity of titanium dioxide, Progress in solid state chemistry 32(1) (2004) 33-177.

[59] H. Tang, K. Prasad, R. Sanjines, P. Schmid, F. Levy, Electrical and optical properties of TiO_2 anatase thin films, Journal of Applied Physics 75(4) (1994) 2042-2047.

[60] E.I. Meletis, X. Nie, F.L. Wang, J.C. Jiang, Electrolytic plasma processing for cleaning and metal-coating of steel surfaces, Surface and Coatings Technology 150(2–3) (2002) 246-256.

[61] R.O. Hussein, X. Nie, D.O. Northwood, A. Yerokhin, A. Matthews, Spectroscopic study of electrolytic plasma and discharging behaviour during the plasma electrolytic oxidation (PEO) process, Journal of Physics D: Applied Physics 43(10) (2010) 105203.

[62] A.J. Bard, Electroanalytical chemistry. Volume 14, Marcel Dekker Inc.,New York, NY; 1986.

[63] S. Aliasghari, Plasma Electrolytic Oxidation of Titanium, (Doctoral dissertation) (2014).

[64] A. Smith, R. Kelton, E. Meletis, Deposition of Ni coatings by electrolytic plasma processing, Plasma Chemistry and Plasma Processing 35(6) (2015) 963-978.

[65] C. Cionea, Microstructural evolution of surface layers during Electrolytic Plasma Processing, The University of Texas at Arlington, ProQuest Dissertations Publishing, (2010) 3408915.

[66] M. Aliofkhazraei, A. Sabour Roohaghdam, A novel method for preparing aluminum diffusion coating by nanocrystalline plasma electrolysis, Electrochemistry Communications 9 (11) (2007) 2686-2691.

[67] M. Aliofkhazraei, A. Sabour Rouhaghdam, A. Heydarzadeh, H. Elmkhah, Nanostructured layer formed on CP-Ti by plasma electrolysis (effect of voltage and duty cycle of cathodic/anodic direction), Materials Chemistry and Physics 113 (2–3) (2009) 607-612.

[68] M. Aliofkhazraei, C. Morillo, R. Miresmaeili, A. Sabour Rouhaghdam, Carburizing of low-melting-point metals by pulsed nanocrystalline plasma electrolytic carburizing, Surface and Coatings Technology 202(22–23) (2008) 5493-5496.

[69] X. Nie, C. Tsotsos, A. Wilson, A.L. Yerokhin, A. Leyland, A. Matthews, Characteristics of a plasma electrolytic nitrocarburising treatment for stainless steels, Surface and Coatings Technology 139(2–3) (2001) 135-142.

[70] P. Taheri, C. Dehghanian, M. Aliofkhazraei, A.S. Rouhaghdam, Nanocrystalline structure produced by complex surface treatments: plasma electrolytic

nitrocarburizing, boronitriding, borocarburizing, and borocarbonitriding, Plasma Processes and Polymers 4 (2007) S721-S727.

[71] C. Wang, F. Wang, Y. Han, Structural characteristics and outward–inward growth behavior of tantalum oxide coatings on tantalum by micro-arc oxidation, Surface and Coatings Technology 214 (2013) 110-116.

[72] M. Petković, S. Stojadinović, R. Vasilić, L. Zeković, Characterization of oxide coatings formed on tantalum by plasma electrolytic oxidation in 12-tungstosilicic acid, Applied Surface Science 257(24) (2011) 10590-10594.

[73] G. Lv, W. Gu, H. Chen, W. Feng, M.L. Khosa, L. Li, E. Niu, G. Zhang, S.-Z. Yang, Characteristic of ceramic coatings on aluminum by plasma electrolytic oxidation in silicate and phosphate electrolyte, Applied Surface Science 253(5) (2006) 2947-2952.

[74] H. Duan, C. Yan, F. Wang, Growth process of plasma electrolytic oxidation films formed on magnesium alloy AZ91D in silicate solution, Electrochimica Acta 52(15) (2007) 5002-5009.

[75] R.O. Hussein, X. Nie, D.O. Northwood, An investigation of ceramic coating growth mechanisms in plasma electrolytic oxidation (PEO) processing, Electrochimica Acta 112 (2013) 111-119.

[76] E. Matykina, A. Berkani, P. Skeldon, G. Thompson, Real-time imaging of coating growth during plasma electrolytic oxidation of titanium, Electrochimica Acta 53(4) (2007) 1987-1994.

[77] K. Venkateswarlu, N. Rameshbabu, D. Sreekanth, A. Bose, V. Muthupandi, N. Babu, S. Subramanian, Role of electrolyte additives on in-vitro electrochemical behavior of micro arc oxidized titania films on Cp Ti, Applied Surface Science 258(18) (2012) 6853-6863.

[78] Y. Yangi, H. Wu, Effects of Current Density on Microstructure of Titania Coatings by Micro-arc Oxidation, Journal of Materials Science & Technology 28(4) (2012) 321-324.

[79] J. Peng, B. Han, W. Li, J. Du, P. Guo, D. Han, Study on the microstructural evolution of $BaTiO_3$ on titanium substrate during MAO, Materials Letters 62(12) (2008) 1801-1804.

[80] Y. Jung, K. Shin, Y. Ko, D. Shin, Surface characteristics and biological response of titanium oxide layer formed via micro-arc oxidation in K_3PO_4 and Na_3PO_4 electrolytes, Journal of Alloys and Compounds 586 (2014) 548-552.

[81] X. Zhang, Z.H. Jiang, Z.P. Yao, Z.D. Wu, Electrochemical study of growth behaviour of plasma electrolytic oxidation coating on Ti6Al4V: Effects of the additive, Corrosion Science 52(10) (2010) 3465-3473.

[82] Z. Yao, P. Su, Q. Shen, P. Ju, C. Wu, Y. Zhai, Z. Jiang, Preparation of thermal control coatings on Ti alloy by plasma electrolytic oxidation in K_2ZrF_6 solution, Surface and Coatings Technology 269 (2015) 273-278.

[83] A. Yerokhin, A. Leyland, A. Matthews, Kinetic aspects of aluminium titanate layer formation on titanium alloys by plasma electrolytic oxidation, Applied Surface Science 200(1) (2002) 172-184.

[84] C. Martini, L. Ceschini, F. Tarterini, J. Paillard, J. Curran, PEO layers obtained from mixed aluminate–phosphate baths on Ti–6Al–4V: Dry sliding behaviour and influence of a PTFE topcoat, Wear 269(11) (2010) 747-756.

[85] J. Wheeler, C. Collier, J. Paillard, J. Curran, Evaluation of micromechanical behaviour of plasma electrolytic oxidation (PEO) coatings on Ti–6Al–4V, Surface and Coatings Technology 204(21) (2010) 3399-3409.

[86] Z. Yao, Y. Jiang, F. Jia, Z. Jiang, F. Wang, Growth characteristics of plasma electrolytic oxidation ceramic coatings on Ti–6Al–4V alloy, Applied Surface Science 254(13) (2008) 4084-4091.

[87] A. Yerokhin, X. Nie, A. Leyland, A. Matthews, S. Dowey, Plasma electrolysis for surface engineering, Surface and Coatings Technology 122(2) (1999) 73-93.

[88] M. Aliofkhazraei, A.S. Rouhaghdam, Wear and coating removal mechanism of alumina/titania nanocomposite layer fabricated by plasma electrolysis, Surface and Coatings Technology 205 (2011) 57-62.

[89] F. Walsh, C. Low, R. Wood, K. Stevens, J. Archer, A. Poeton, A. Ryder, Plasma electrolytic oxidation (PEO) for production of anodised coatings on lightweight metal (Al, Mg, Ti) alloys, Transactions of the IMF 87 (2013) 122-135.

[90] R. Khan, A. Yerokhin, T. Pilkington, A. Leyland, A. Matthews, Residual stresses in plasma electrolytic oxidation coatings on Al alloy produced by pulsed unipolar current, Surface and Coatings Technology 200(5) (2005) 1580-1586.

[91] V. Dehnavi, Surface modification of aluminum alloys by plasma electrolytic oxidation, The University of Western Ontario, (2014) Electronic Thesis and Dissertation Repository 2311.

[92] L. Chang, Growth regularity of ceramic coating on magnesium alloy by plasma electrolytic oxidation, Journal of Alloys and Compounds 468(1–2) (2009) 462-465.

[93] E. Matykina, R. Arrabal, F. Monfort, P. Skeldon, G. Thompson, Incorporation of zirconia into coatings formed by DC plasma electrolytic oxidation of aluminium in nanoparticle suspensions, Applied Surface Science 255(5) (2008) 2830-2839.

[94] R.G. Ehl, A.J. Ihde, Faraday's electrochemical laws and the determination of equivalent weights, J. Chem. Educ 31(5) (1954) 226.

[95] E. Matykina, R. Arrabal, P. Skeldon, G.E. Thompson, Transmission electron microscopy of coatings formed by plasma electrolytic oxidation of titanium, Acta Biomaterialia 5(4) (2009) 1356-1366.

[96] J.J. Moore, Chemical metallurgy 2nd edition , Elsevier (2013).

[97] K.R. Shin, Y.S. Kim, G.W. Kim, Y.G. Ko, D.H. Shin, Development of titanium oxide layer containing nanocrystalline zirconia particles with tetragonal structure: Structural and biological characteristics, Colloids and Surfaces B: Biointerfaces 131 (2015) 47-53.

[98] K.J.A. Raj, R. Shanmugam, R. Mahalakshmi, B. Viswanathan, XPS and IR spectral studies on the structure of phosphate and sulphate modified titania-A combined DFT and experimental study, Indian J Chem A 49 (2010) 9-17.

[99] H.F. Guo, M.Z. An, H.B. Huo, S. Xu, L.J. Wu, Microstructure characteristic of ceramic coatings fabricated on magnesium alloys by micro-arc oxidation in alkaline silicate solutions, Applied Surface Science 252(22) (2006) 7911-7916.

[100] C. Viornery, Y. Chevolot, D. Léonard, B.-O. Aronsson, P. Péchy, H.J. Mathieu, P. Descouts, M. Grätzel, Surface modification of titanium with phosphonic acid to improve bone bonding: characterization by XPS and ToF-SIMS, Langmuir 18(7) (2002) 2582-2589.

[101] A. Puziy, O. Poddubnaya, A. Ziatdinov, On the chemical structure of phosphorus compounds in phosphoric acid-activated carbon, Applied surface science 252(23) (2006) 8036-8038.

[102] J. Liu, J. Zhang, S. Cheng, Z. Liu, B. Han, DNA-Mediated Synthesis of Microporous Single-Crystal-Like $NaTi_2(PO_4)_3$ Nanospheres, small 4(11) (2008) 1976-1979.

[103] K. Elghniji, M. Saad, M. Araissi, E. Elaloui, Y. Moussaoui, Chemical modification of TiO_2 by $H_2PO_4^-/HPO_4^{2-}$ anions using the sol-gel route with controlled precipitation and hydrolysis: enhancing thermal stability, Materials Science-Poland 32(4) (2014) 617-625.

[104] J. Liang, B. Guo, J. Tian, H. Liu, J. Zhou, W. Liu, T. Xu, Effects of $NaAlO_2$ on structure and corrosion resistance of microarc oxidation coatings formed on AM60B magnesium alloy in phosphate–KOH electrolyte, Surface and Coatings Technology 199(2) (2005) 121-126.